INELASTIC STRAIN ANALYSIS OF SOLDER JOINT

IN

NASA FATIGUE SPECIMEN

Final Report

Grant No. NAG 5-1331
NASA Goddard Space Flight Center

CALCE Center for Electronics Packaging
University of Maryland
College Park, MD 20742

INELASTIC STRAIN ANALYSIS OF SOLDER JOINT IN NASA FATIGUE SPECIMEN

January 28, 1991

Final Report

Grant No. NAG 5-1331

NASA Goddard Space Flight Center

Prepared by

Abhijit Dasgupta

Chen Oyan

CALCE Center for Electronic Packaging

Mechanical Engineering Department

University of Maryland

College Park, MD 20742

TABLE OF CONTENTS:

Section	Page
List of Tables	iii
List of Figures	iv
Abstract	1
Introduction	2
Analysis	4
Results & Discussion	7
Conclusion	14
Recommendations For Future Work	15
References	16
Acknowledgements	17

LIST OF TABLES:

Number		Page
Table 1 :	Linear elastic properties of materials in the solder fatigue specimen.	18
Table 2 :	Nonlinear properties of materials in the solder fatigue specimen.	19

LIST OF FIGURES :

Number		Page
Figure 1	: Axisymmetric finite element discretization of solder fatigue specimen.	20
Figure 2	: Enlarged view of mesh discretization in solder.	21
Figure 3	: Temperature histories for specimen loading.	22
Figure 4	: Deformed mesh at temperature change of 31° C.	23
Figure 5a	: Solder deformation after loading to T=55.5° C.	24
Figure 5b	: Solder deformation after 20 min. dwell at T=55.5° C	25
Figure 5c	: Solder deformation after unloading to T=24.5° C.	26
Figure 5d	: Solder deformation after 20 min. dwell at T=24.5° C.	27
Figure 6a	: Maximum shear strain in solder after loading to T=55.5° C	28
Figure 6b	: Maximum shear strain in solder after 20 min. dwell at T=55.5° C.	29
Figure 6c	: Maximum shear strain in solder after unloading to T=24.5° C.	30
Figure 6d	: Maximum shear strain in solder after 20 min. dwell at T=24.5° C.	31
Figure 7	: Maximum principal strain in solder after 20 min. dwell at T=24.5° C.	32

Number		Page
Figure 8	: Maximum shear strain history at nodes 260 and 30 for two cycles at cyclic temperature change of 31° C.	33
Figure 9a	: Elastic equivalent strain history at nodes 260 and 30 for two cycles at a cyclic temperature change of 31° C.	34
Figure 9b	: Plastic equivalent strain history at nodes 260 and 30 for two cycles at a cyclic temperature change of 31° C.	35
Figure 9c	: Creep equivalent strain at nodes 260 and 30 for two cycles at a cyclic temperature change of 31° C.	36
Figure 10a	: Hysteresis loop at node 260 for two cycles at a cyclic temperature change of 31° C.	37
Figure 10b	: Hysteresis loop at node 30 for two cycles at a cyclic temperature change of 31° C.	38
Figure 11a	: Solder deformation after loading to T=96.5° C.	39
Figure 11b	: Solder deformation after 20 min. dwell at T=96.5° C.	40
Figure 11c	: Solder deformation after unloading to T=-16.5° C.	41
Figure 11d	: Solder deformation after 20 min. dwell at T=-16.5° C.	42
Figure 12a	: Maximum shear strain in solder after loading to T=96.5° C.	43
Figure 12b	: Maximum shear strain an solder after 20 min. dwell at T=96.5° C.	44

Number **Page**

Figure 12c : Maximum shear strain in solder after unloading to T=-16.5° C. 45

Figure 12d : Maximum shear strain in solder after 20 min. dwell at T=-16.5° C. 46

Figure 13 : Maximum principal strain in solder after 20 min. dwell at T=-16.5° C. 47

Figure 14 : Maximum shear strain history at node 260 and 30 for two cycles at cyclic temperature change of 113° C. 48

Figure 15a : Elastic equivalent strain history at node 260 and 30 for two cycles at cyclic temperature change of 113° C. 49

Figure 15b : Plastic equivalent strain history at node 260 and 30 for two cycles at cyclic temperature change of 113° C. 50

Figure 15c : Creep equivalent strain history at node 260 and 30 for two cycles at cyclic temperature change of 113° C. 51

Figure 16a : Hysteresis loop at node 260 for two cycles at a cyclic temperature change of 113° C. 52

Figure 16b : Hysteresis loop at node 30 for two cycles at a cyclic temperature change of 113° C. 53

1. ABSTRACT:

The solder fatigue specimen designed by NASA-GSFC/UNISYS is analyzed in order to obtain the inelastic strain history during two different representative temperature cycles specified by UNISYS. In previous reports (dated July 25, 1990 & November 15, 1990), results were presented of the elastic-plastic and creep analysis for $\Delta T=31^{\circ}$ C cycle ,respectively. The present report summarizes subsequent results obtained during the current phase, from visco-plastic finite element analysis of the solder fatigue specimen for $\Delta T=113^{\circ}$ C cycle. Some common information is repeated here for self-completeness. Large-deformation continuum formulations in conjunction with a standard linear solid model is utilized for modeling the solder constitutive creep-plasticity behavior. Relevant material properties are obtained from the literature. Strain amplitudes,mean strains, and residual strains (as well as stresses) accumulated due to a representative complete temperature cycle are obtained as a result of this analysis. The partitioning between elastic strains, time-independent inelastic (plastic) strains, and time-dependent inelastic (creep) strains is also explicitly obtained for two representative cycles. Detailed plots are presented in this report for two representative temperature cycles.This information forms an important input for fatigue damage models, when predicting the fatigue life of solder joints under thermal cycling.

2. INTRODUCTION :

Solder fatigue in electronic package is a major cause for poor reliability and premature failures under thermo-mechanical loading. The fatigue damage results from cyclic mechanical strains induced by a combination of (i) TCE mismatch between the dissimilar components connected together by the solder, and (ii) vibrational loads. Since solder is a highly visco-plastic material over typical operating temperature ranges, slow thermal cycling produces primarily anelastic (creep) strains and relatively negligible amounts of elastic and plastic strains. On the other hand, vibrational loads are of a much higher frequency and cause primarily elastic and plastic strains and relatively little anelastic strains. The partitioning between the different types of strains (elastic, plastic and anelastic) is dependent on the mean operational temperature, the stress levels and the respective dwell times to which the joint is exposed.

In order to obtain simplified closed-form models, it is common practice to ignore the strain range partitioning between the elastic, plastic and creep strains, and to use the total strain amplitude instead as a loading parameter, when computing fatigue life from the Coffin-Manson model [1]. However, Solomon has illustrated in a comprehensive set of experiments that it is not possible to extrapolate the same damage constants to low operating temperatures [2]. One solution is to apply Halford & Manson's strain range partitioning technique [3]. Similar approaches have been used successfully by Knecht, Fox and Shine [4,5] in the past for modeling creep-fatigue interations in solder material. It is necessary, therefore, to account for the partitioning between the elastic, plastic and

anelastic components of strains, if accurate life predictions are desired.

The purpose of this study is to conduct a detailed analysis of the inelastic strain history of a sample solder joint under different thermal cycles. Particular attention is paid to the strain-range partitioning. The geometry chosen for the analysis is the experimental specimen designed by UNISYS/NASA-GSFC for the solder fatigue program. A numerical finite element analysis is utilized, in view of the complex geometry.

3. ANALYSIS :

The analysis is conducted using the MARC general-purpose commerical FEM code developed and marketed by Dr. Marcal and his associates. This program is an excellent research tool and not only has more versatile nonlinear capabilities than ANSYS, but also licences the analysis of larger models within the educational environment. Pre- and Post-Processing is done on PATRAN in view of its excellent interative graphics and user-friendly software environment.

The specimen consists of brass pins soldered into copper plated through holes (PTH) on a FR4 PWB. The brass pins have a circular shoulder/flange and are immersed in a thermosetting epoxy. As the board is temperature-cycled, the differential expansion between the epoxy and the brass pin causes an axial tensile load on the brass pin, thereby loading the solder in shear. Shear stresses are also generated due to the CTE mismatch between the brass pin and the PTH in the axial direction. Superposed on this shear load are extensional hoop and radial stresses (& strains) in the solder, due to differential expensions of the brass, solder, copper and FR4 in the radial direction.

Figure 1 shows the axisymmetric finite element mesh generated to model the specimen assembly. The brass pin is color coded blue, solder is shown in yellow, copper in red, FR4 in green and epoxy in pink. The total mesh consists of 476 elements and 530 nodes. Figure 2 shows an enlarged view of the finite element discretization of the solder material, consisting of 80 elements and 102 nodes. All subsequent strain plots are shown for this region of interest only.

The woven-fabric FR4 board is treated approximately as transversely isotropic, with the plane of the board being the plane of isotropy. All other materials are treated as isotropic. The board and the epoxy are treated as linear elastic within the temperature range of this analysis since the maximum temperature is always maintained below the glass-transition temperature Tg of the resin in the FR4 board.

All materials except the FR4 PWB board material and the epoxy are treated as power-law hardening elastic-plastic materials with a Ramberg-Osgood type constitutive model given in equation (1).

$$\varepsilon = \varepsilon_{el} + \varepsilon_{pl} = \sigma/E + (\sigma/K)^{1/n} \qquad (1)$$

where E is the elastic modulus, σ is the stress, K is the Ramberg-Osgood constant and n is the strain-hardening exponent.

Creep behavior of the solder is modeled with a Weertman steady state creep law. Thus, the strain rate is assumed to have a power-law dependence on the stress magnitude and an exponential dependence on the inverse of the absolute temperature as shown in equation (2).

$$\varepsilon_{cr} = C_1 \sigma^{C_2} e^{-C_4/T} t \qquad (2)$$

where C_1, C_2, C_4 are material properties, σ is the stress, T is the absolute temperature and t is the elapsed time.

Linear material properties are listed in Table 1 and nonlinear material properties are given in Table 2. Copper, brass and epoxy properties are obtained from ASM

Handbooks. FR4 properties have been generated by this research group during a related study [6]. Elastic-plastic solder properties are obtained from Westinghouse test reports [7] and creep properties for the solder are obtained from a study conducted by Tribula & Morris [8] for 60Pb-40Sn solder.

The entire assembly is subjected to two different temperature cycles, specified by UNISYS/NASA-GSFC, as shown in Figure 3. Both cycles have a mean temperature of 40° C. The temperature ranges are 31° C and 113° C, respectively. Loading and unloading rates are 6° C per minute, and 20 minute dwells are provided at both extremes of the cycle. In order to facilitate creep computations, the temperature loading and unloading phases are idealized as step functions followed by dwells equal to the time taken for the loading/unloading. It is noted that this simplification yields a conservative over-estimate of the resulting strains. Incremental load stepping techniques are used since the strains are well beyond the elastic limit of the solder. The 20 minute dwells are modeled with appropriate time stepping techniques. Finite deformation formulations are used throughout the study in order to model the large deformations, strains and rotations. Two complete loading and unloading cycles are modeled for each of the two representative temperature cycles shown in Figure 3. The purpose of modeling two strain cycles is to observe the effects of rachetting and shakedown as the hysteresis cycles approach a stable steady-state configuration. Appropriate nodal constraints are applied to constrain rigid body motions and to simulate far-field mechanical constraints. No other mechanical loads are applied.

4. RESULTS & DISCUSSIONS :

4.1 LOAD CYCLE 1 :

The first load cycle considered is the cycle with the smaller temperature range of 31° C. Figure 4 shows a plot of the elastic deformations of the entire structure. Figures 5a through 5d show plots of the deformed geometry of the solder at four different milestones during the first cycle. Figure 5a shows a plot at the highest temperature (55.5° C) during the loading cycle, superposed on the undeformed plot. Figure 5b through 5d show similar plots of the deformed solder geometry at the end of the 20 minute dwell at T_{max}, after unloading to T_{min} (24.5° C), and after the 20 minute dwell at T_{min}, respectively.

Contour plots of the maximum shear strains at the four milestones indicated above, are shown in figures 6a through 6d. These figures clearly illustrate the strain concentration around the fillet at the interface between the brass pin, solder and the epoxy (node 260 in the finite element model, as illustrated in figure 2). The maximum strain concentration remains at this site throughout most of the cycle duration. The residual strain field after unloading, shown in figure 6c, still shows this strain concentration, indicating that this site undergoes the maximum strain cycling and hence accumulates the maximum fatigue damage. Finally, during the dwell at T_{min}, the strain concentration site shifts marginally away from the interface. More importantly, another strain concentration site develops at the opposite corner around node 30, indicating that the strain history at this node may also be of interest from a fatigue damage perspective. Clearly, the node that suffers maximum strain cycling and rachetting is node number 260 (see figure 2). Figure 7 shows that

similar conclusions may also be inferred for the maximum principal strain. This conclusion has been verified to be true for all other strain and stress components. For reasons of brevity, those contour plots are not included in this report. Figure 7 also illustrates that the maximum principal strain is almost half as large as the maximum shear strain, indicating the significant multiaxiality of the strain (and stress) fields.

Figure 8 shows the maximum shear strain history at the most severe locations (nodes 260 & 30) for the first two cycles at this load amplitude. The figure illustrates several very important features of the deformations. Node 260 undergoes both rachetting and shakedown after the first temperature cycle. Consequently, the strain amplitude is much smaller during the second cycle. The maximum shear strain is about 37,000 microstrain for the first cycle and increases to about 40,000 microstrain during the second cycle due to rachetting effects. The shakedown effect reduces the strain amplitude from about 18,000 microstrain during the first cycle to less than 10,000 microstrain by the second cycle. Node 30 experiences an even greater amount of rachetting and shakedown. Consequently, the strain amplitude during the second cycle is almost zero, though the maximum strain is almost 28,000 microstrain. The shear strain at nodes 260 and 30 are of comparable magnitudes but of opposite signs. However, the figure clearly illustrates that the cyclic strain amplitude (and hence fatigue damage) is much larger at node 260 than at node 30.

Figures 9a through 9c present the graphs which constitute part of the main deliverables in this study, viz. partitioned elastic, plastic and anelastic (creep) strain histories for one of the given load cycles. The equivalent strain (also called the Von Mises' strain or

of the given load cycles. The equivalent strain (also called the Von Mises' strain or distortional energy strain or the octahedral shear strain) is chosen for these plots because of the multiaxiality of the strain field. Figures 9a and 9b clearly show that the cyclic elastic and plastic strain amplitudes are much larger at node 260 than at node 30. The elastic strain is almost completely reversed at node 260 while the plastic strain component has a significant mean value (approximately 2,100 microstrain during the first cycle and 1,800 microstrain during the second). The maximum plastic strain of 3,200 microstrain is almost twice the maximum elastic strain while the amplitude of plastic strain is almost the same as the elastic strain amplitude (approximately 1,600 microstrain). Figure 9c shows that the creep strain amplitudes and mean values are significantly higher than the elastic and plastic strain values. The maximum creep strain at nodes 260 and 30 are comparable in magnitude but the amplitude at node 30 is almost negligible while the amplitude at node 260 is approximately 5,000 microstrain. Creep rachetting and shakedown effects are both evident at node 260. The residual strains at the end of second cycle clearly have a combination of elastic, plastic and creep components.

4.2 LOAD CYCLE 2 :

The temperature range of 113° C for this load history is much larger than the first load cycle of 31° C temperature range. The results are qualitatively similar to the results in section 4.1. However, the strain amplitudes are much higher and the maximum strain concentration in this loading cycle shifts to the opposite corner creating a possible site of creep rupture due to excessive rachetting.

at four different milestones during this large temperature cycle. Figure 11a shows a plot at the highest temperature (96.5° C) during the loading cycle, superposed on the undeformed plot. Figures 11b through 11d show similar plots of the deformed solder geometry at the end of the 20 minute dwell at T_{max}, after unloading to T_{min} (-16.5° C) and after the 20 minute dwell at T_{min}, respectively.

Contour plots of the maximum shear strains at the four milestones indicated above, are shown in figures 12a through 12d. In this loading cycle, unlike in the $\Delta T=31_0$ C cycle, the strain concentration changes its site from node 260 to node 30 which is located at the interface between the solder and at the free end of copper PTH. The maximum strain concentration remains at node 30 through most of the cycle duration. The residual strain field after unloading shown in Figure 12c also illustrates this strain concentration, indicating that this site (node 30) experiences the maximum strain amplitude and accumulates the maximum creep strain. Finally, during the dwell at T_{min}, the position of strain concentration still remains the same indicating that the failure will begin due to creep rupture at node 30. Figure 13 shows that similar conclusions can be drawn about the maximum principal strain. Similar results have been verified to be true for all other strain and stress components. For brevity, those contour plots are not included in the report. Figure 13 also illustrates that the maximum principal strain is almost half as large as the maximum shear strain, indicating again the significant multiaxiality of the strain (and stress) fields.

Figure 14 shows the maximum shear strain history at the representative locations (nodes 260 and 30) for the first two cycles at this load amplitude. Nodes 260 and 30 both

(nodes 260 and 30) for the first two cycles at this load amplitude. Nodes 260 and 30 both undergo rachetting after the first temperature cycle leading to an accumulation of inelastic strains. Further, the strain amplitude is smaller during the second cycle due to shakedown effects. The maximum shear strain occuring at node 30 is about 195,000 microstrain for the first cycle and increases to about 280,000 microstrain during the second cycle due to rachetting effects and this amount is far larger than that at node 260 which the maximum value is just about 110,000 microstrain for the first cycle and about 150,000 microstrain for the second cycle due to the rachetting effect. The shakedown effect reduces the strain amplitude of node 260 from about 58,000 microstrain during the first cycle to less than 25,000 microstrain by the second cycle. However, node 30 experiences an even greater amount of rachetting and shakedown. Therefore, the strain amplitude during the second cycle is nearly zero though the maximum strain is almost 280,000 microstrain. This figure clearly illustrates that the cyclic strain amplitude and mean strains are much larger at node 30 than at node 260. Consequently, failure will occur at node 30 due to creep rupture rather than due to fatigue damage at node 260.

Figures 15a through 15c present the graphs which constitute part of the main deliverables in this study, viz. partitioned elastic, plastic and anelastic (creep) strain histories for $\Delta T=113^{\circ}$ C cycle. The elastic strain is almost completely reversed at node 260 while this condition does not occur at node 30 that suffers the effect of rachetting. The plastic strain component at node 260 has a mean value of about 2,500 microstrain during the first cycle and about -8,500 microstrain during the second cycle. The maximum plastic strain of 14,000 microstrain is almost five times larger than the maximum elastic

strain at node 30 while the amplitude of plastic strain (about 11,000 microstrain) is also almost five times larger than the elastic strain amplitude (about 2,200 microstrain) at node 260. Figure 15c shows that the creep strain amplitudes and mean values are significantly higher than the elastic and plastic strain values. The maximum creep strain at node 260 and node 30 are of comparable magnitude but the amplitude at node 30 is almost negligible while the amplitude at node 260 is approximately 5,000 microstrain. Creep rachetting and shakedown are both evident at nodes 260 and 30. The residual strain at the end of the second cycle clearly has a combination of elastic, plastic and creep components.

Figures 15a & 9a also show that the stresses (which are related to the elastic strains) are not constant during the creep phase. This is better illustrated in figures 16a, 16b and figures 10a, 10b which show the hysteresis loops during the first two load cycles. Figure 16a clearly illustrates that the rachetting is significant during the first cycle but is almost halted during the second cycle at node 260. By the end of the second cycle, the hysteresis loop reaches an almost stable and steady state configuration. The strain amplitude is much smaller during the second cycle than the first cycle due to the shakedown effects. Figure 16b shows that rachetting is monotonically continuous though at a decreasing rate. Hence the failure mode for this configuration is likely to be by creep rupture due to excessive accumulation of creep strains at node 30.

Figures 16a, 16b and figures 10a, 10b further illustrate the fact that the creep deformations are accompanied by stress relaxation. This raises serious doubts about the validity of using a conventional Halford-Manson type strain-range partitioning techniques

for fatigue damage evaluation, since the fatigue constants for the conventional creep-fatigue models are usually obtained under constant stress conditions in laboratory specimens. An alternative fatigue law is therefore required to deal with the present situations. For instance, though the creep strain amplitude is larger at node 30 than at node 260, the inelastic energy dissipation is larger at node 260 than at node 30. Thus energy-based and strain-based failure laws will produce conflicting predictions of fatigue damage accumulation for this load cycle. Clearly, further work is warranted to clarify these issues conclusively.

5. CONCLUSION :

A detailed elastic-plastic-anelastic strain analysis has been conducted for the solder in the specimen. Histories of the elastic-plastic and anelastic components of strain have been obtained in partitioned form. It is evident from this study that when the temperature range is small the failure of solder will result from the fatigue damage at the fillet at the interface with the epoxy and the brass pin, since the strain amplitude range are highest at this site. With the increase of temperature range as seen from 31° C to 113° C, not only do all strain components increase, but also the maximum strain concentration will shift to the opposite diagonal corner located at the interface of solder and copper PTH and result in failure due to creep rupture, rather than due to fatigue.

This study also reveals that the state of strain is multiaxial rather than one of pure shear. It is necessary therefore to utilize a multidimensional fatigue damage law rather than a simple shear fatigue damage law.

The partitioning between the elastic, plastic and creep strains have been clearly illustrated. Such information is required for successful implementation the creep-fatigue damage interactions. However, it is pointed out that a conventional partitioning method of the Halford-Manson type is not possible here since the stresses are continually relaxing during the creep deformation and are not held constant as is required for the Halford-Manson model to be valid. It is clearly necessary therefore to develop a more sophisticated and more generalized creep-fatigue damage interaction model, in order to handle the present situation.

6. RECOMMENDATIONS FOR FUTURE WORK :

This study clearly illustrates that in order to obtain a successful interpretation of NASA's fatigue program, a more generalized fatigue damage model needs to be developed. This model should have the following attributes:

(i) The model should be capable of accounting for multiaxial strain states. Thus the fatigue life should be formulated in terms of a valid strain measure which characterizes not only the magnitude of the strain but also the multiaxiality.

(ii) The model should be capable of modeling creep-fatigue interactions in a multiaxial strain state, for generalized creep deformations when the strain and stress are both simulaneously changing. Traditional strain-partitioning techniques resort to empirical data collected under constant-stress creep-fatigue tests. Such methods are inappropriate in the present situation and a new model, based on energy partitioning concepts, is required for successful completion of NASA's fatigue program.

7. REFERENCES :

1. Engelmaier, W., "Functional Cycles and Surface Mounting Attachment Reliability," ISHM Technical Monograph Series 6984-002, ISHM, Silver Spring, MD, October, 1984, pp 87-114.

2. Solomon, H, "Influence of Temperature on the Fatigue of CC/PWB joints ," Journal of the IES, Institute of the Environmental Sciences, Mt. Prospect, I1, Vol XXXIII, No. 1, Jan/Feb 1990.

3 Manson, S. S., "The Challenge to Unify Treatment of High Temperature Fatigue - A partisan Proposal Based on Strain Range Partitioning," ASTM STP 520, American Society for Testing and Materials, Philadelphia, PA, 1973.

4. Shine, M. C. Fox, L. R., and Sofia, J. W., "A Strain-Range Partitioning Procedure for Solder Fatigue," Proc., IEPS 4th Annual Intl. Electronics Packaging Conf., Baltimore, MD, Oct. 1984.

5. Knecht, S. and Fox, L.R., "Constitutive Relation and Creep-Fatigue Life model for Eutectic Tin-Lead Solder," IEEE, Components, Hybrids & Manufacturing Technology, June 1990.

6. Dasgupta, A., Bhandarkar, S., Pecht, M. and Barker, D., "Thermoelastic Properties of Woven Fabric Composites Using Homogenization Techniques," 5th Conference of the American Society for Composites, E. Lansing, MI, June, 1990.

7. Private communication, Westinghouse Electric Corpn., Defence Electronics Division, Baltimore, MD.

8. Tribula, D. and Morris, J. W.,"Creep Shear of Experimental Solder Joints," ASME Winter Annual Meeting, 89-WA/EEP-30, San Francisco, CA, Dec., 1989.

8. ACKNOWLEDGMENTS :

The analysis presented here was conducted by Chen Oyan, a graduated student in the Mechanical Engineering department and a member of the Computer Aided Life Cycle Engineering Center for Electronic Packaging. Computing facilities were provided by the CAD Lab of the Mechanical Engineering Department. We also thank John Evans of UNISYS for making this project possible and for his invaluable technical inputs throughout the duration of this study.

TABLE 1

MATERIAL PROPERTIES

LINEAR ELASTICITY

MATERIAL	ELASTIC MODULUS (E:psi)	SHEAR MODULUS (G:psi)	POISSON RATIO (υ)	THERMAL EXP. COEFFICIENT (α:in/in/°C)
COPPER	15.6×10^{6}	5.80×10^{6}	0.355	16.5×10^{-6}
BRASS	15.0×10^{6}	5.64×10^{6}	0.33	20.8×10^{-6}
EPOXY	5.0×10^{5}	1.83×10^{5}	0.37	70.0×10^{-6}
SOLDER	3.62×10^{6}	1.29×10^{6}	0.4	21.0×10^{-6}
FR4	IN-PLANE			
	2.084×10^{6}	8.99×10^{5}	0.159	20.62×10^{-6}
	OUT-OF-PLANE			
	1.0×10^{6}	3.03×10^{5}	0.24	68.31×10^{-6}

TABLE 2

MATERIAL PROPERTIES

NONLINEAR : PLASTICITY & ANELASTICITY

MATERIAL	YIELD STRENGTH (σ_y:psi)	STRENGTH COEFFICIENT (K:psi)	STRAIN-HARDENING EXPONENT (n)	CREEP CONSTANTS (C_i)
COPPER	10,000	46,400	0.54	
BRASS	21,000	130,000	0.49	
SOLDER	4,960	7,025	0.056	$C_1=6.82\text{x}10^{-15}$ $C_2=6.28$ $C_4=8165.2$

† Ramberg Osgood plasticity equation : $\varepsilon_{pl} = (\sigma/K)^{1/n}$

‡ Weertman Creep equation : $\varepsilon_{cr} = C_1\sigma^{C2}\, e^{-C4/T}\, t$

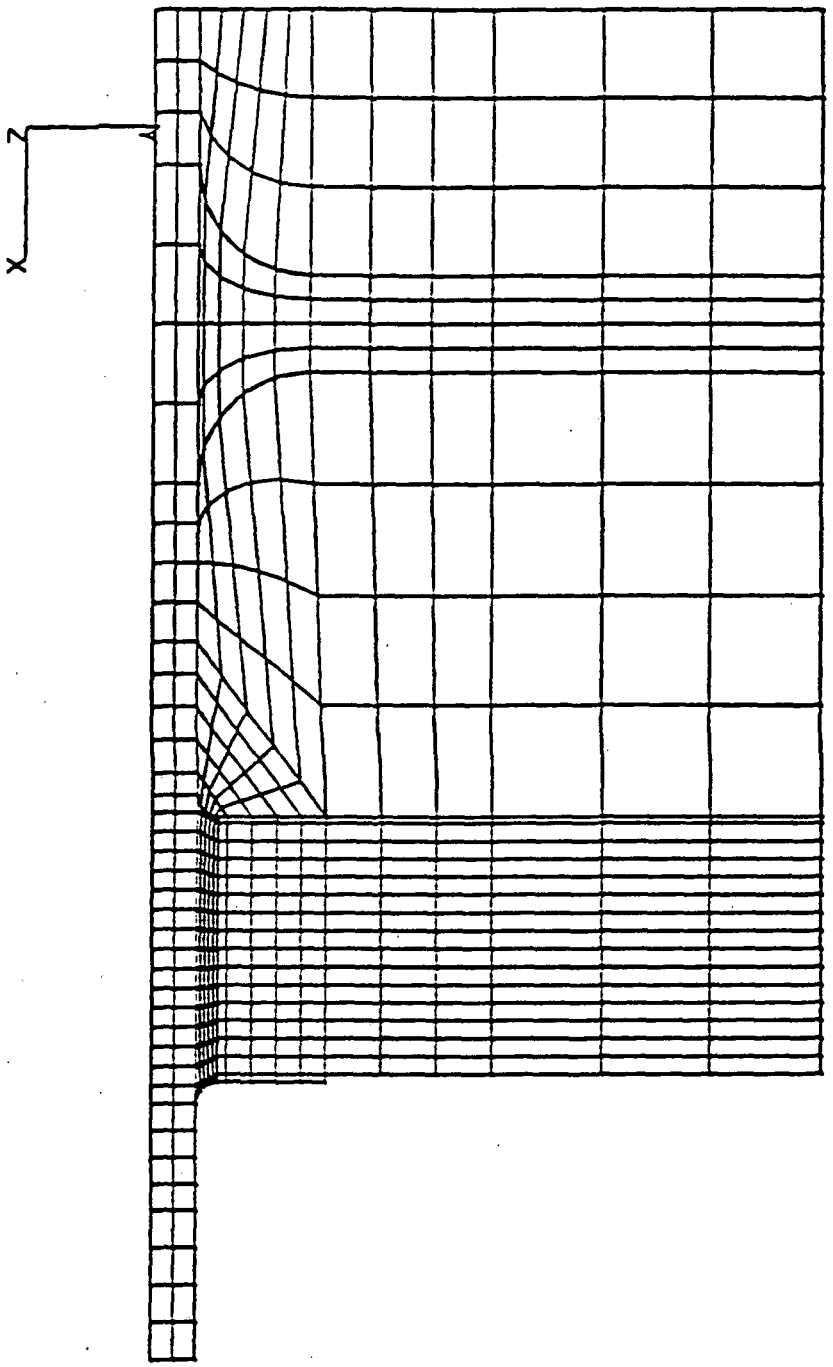

Figure 1: Axisymmetric finite element discretization of solder fatigue specimen.

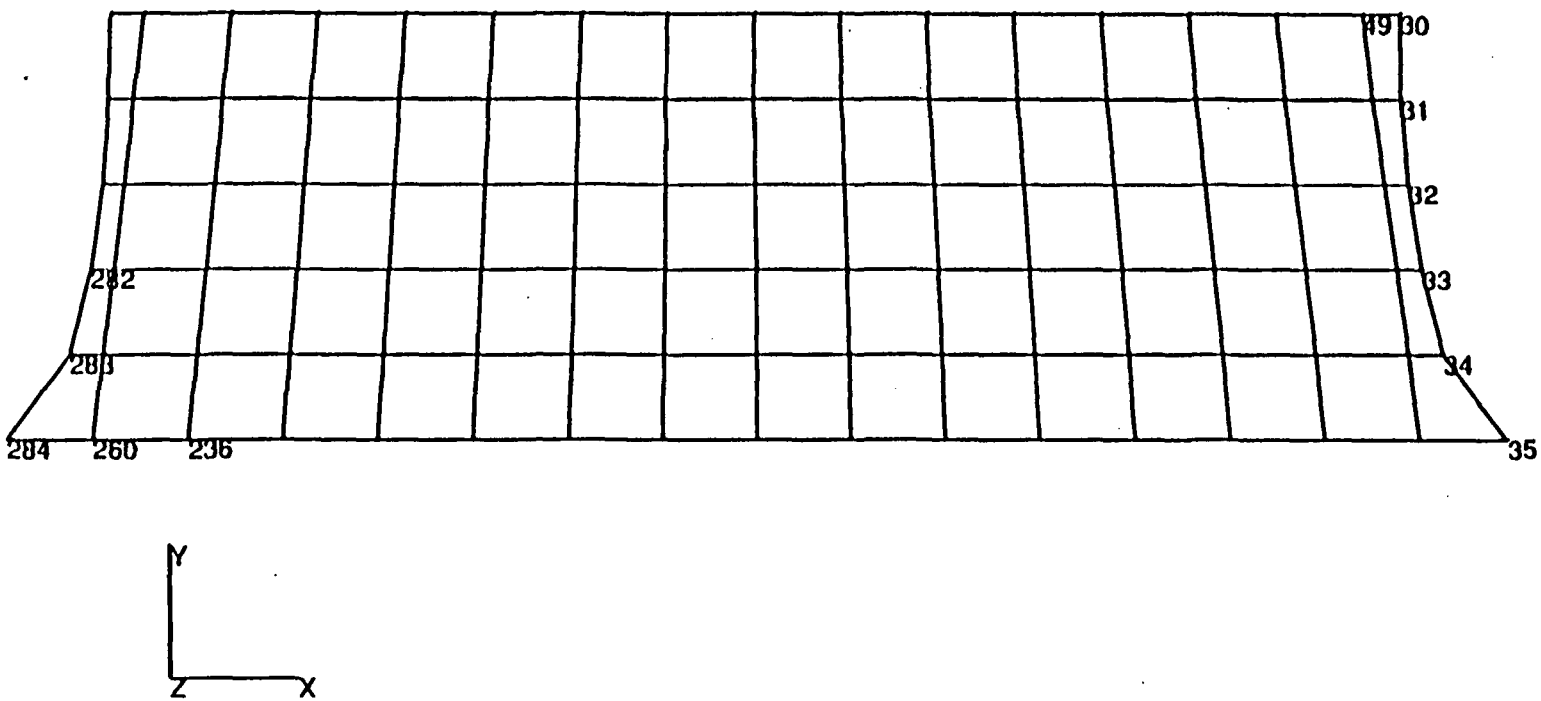

Figure 2: Enlarged view of mesh discretization in solder.

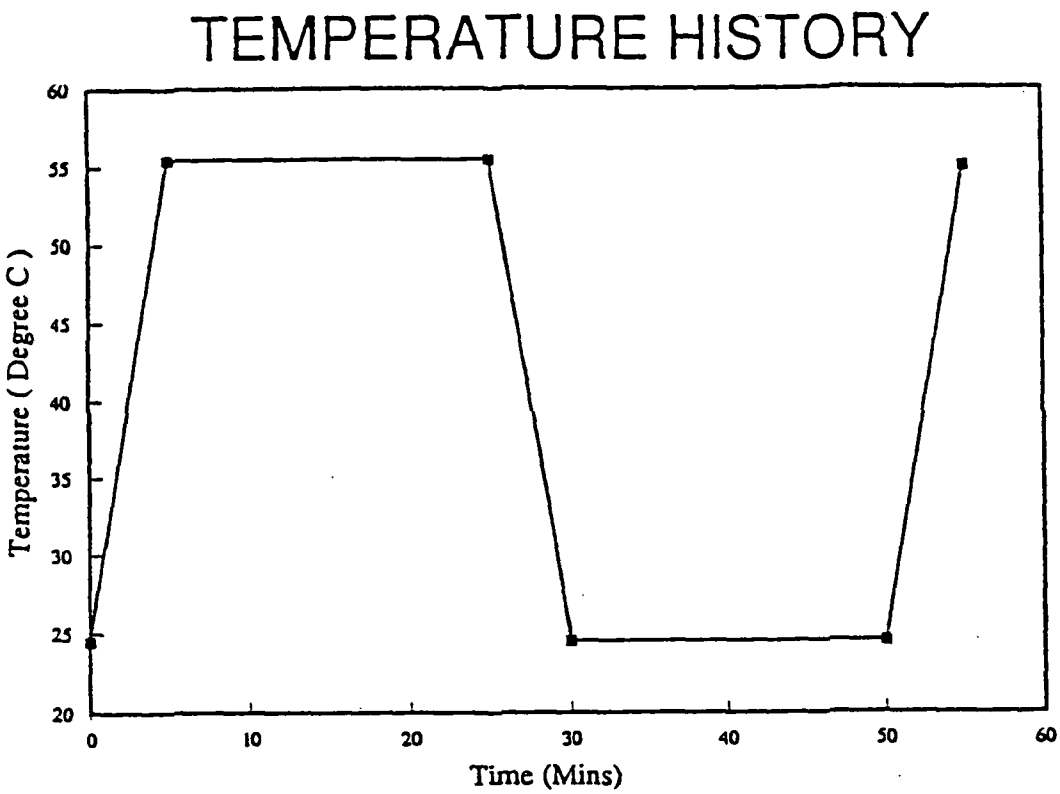

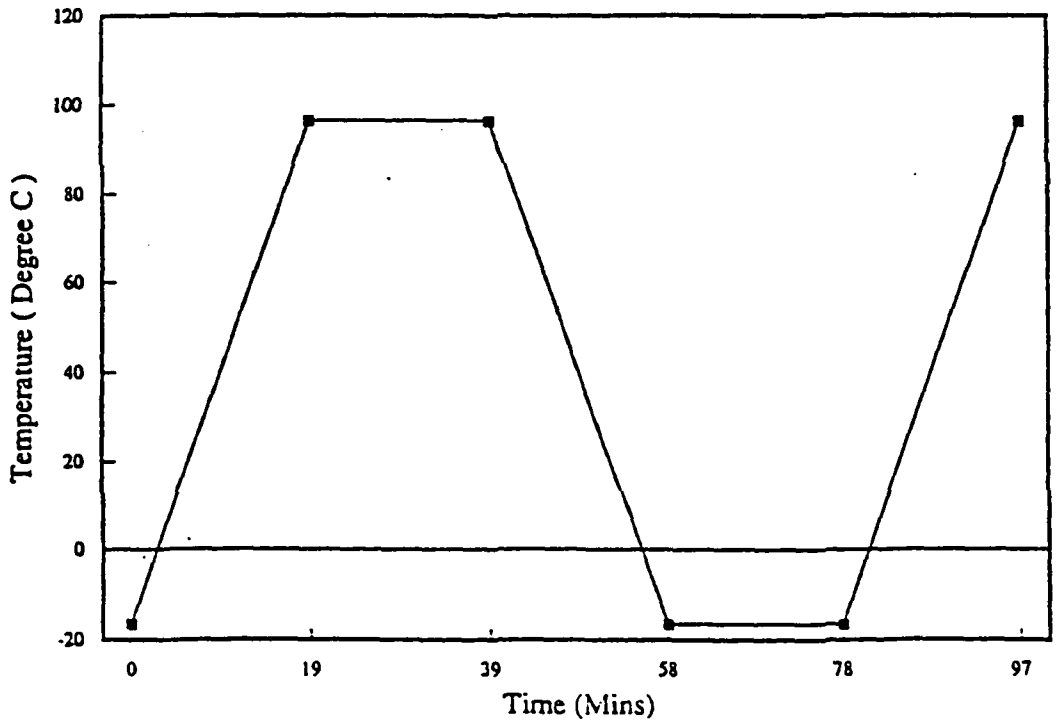

Figure 3: Temperature histories for specimen loading.

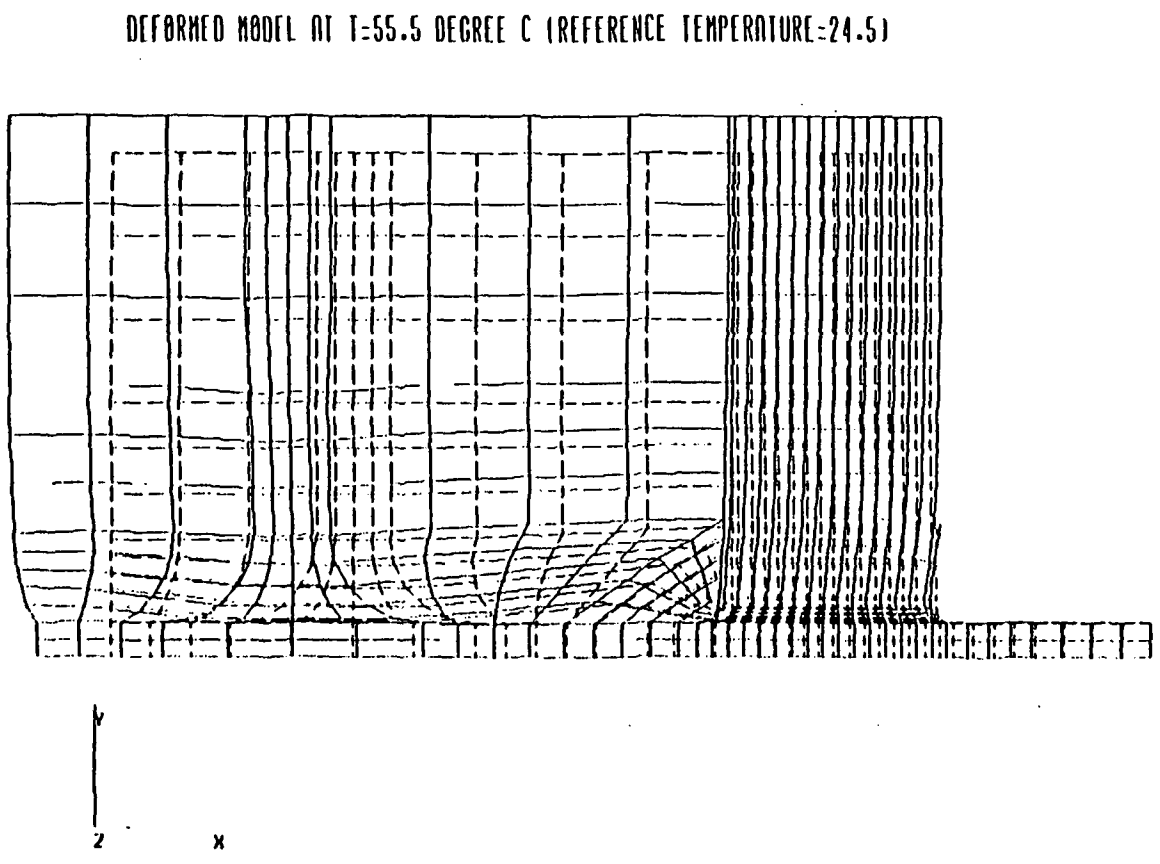

Figure 4: Deformed mesh at temperature change of 31° C.

DISPLACEMENT OF SOLDER AT T=55.5 DEGREE C FOR 31 DEGREE CYCLE

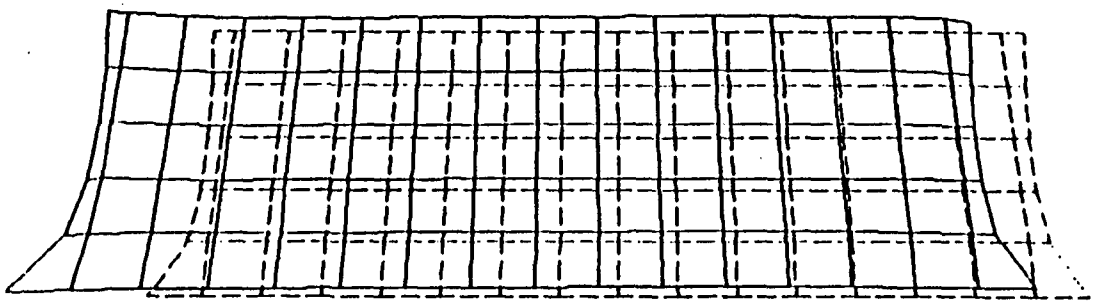

PROJECT CREEP
PATRAN POST-PROCESS FILE CREATED BY MAKPAT1.H 14-JUL-98 17:24:4
TIME = 0.000000E+00 FREQUENCY = 0.000000E+00 GENERALIZED MASS = 0.000

Figure 5a: Solder deformation after loading to T = 55.5°C.

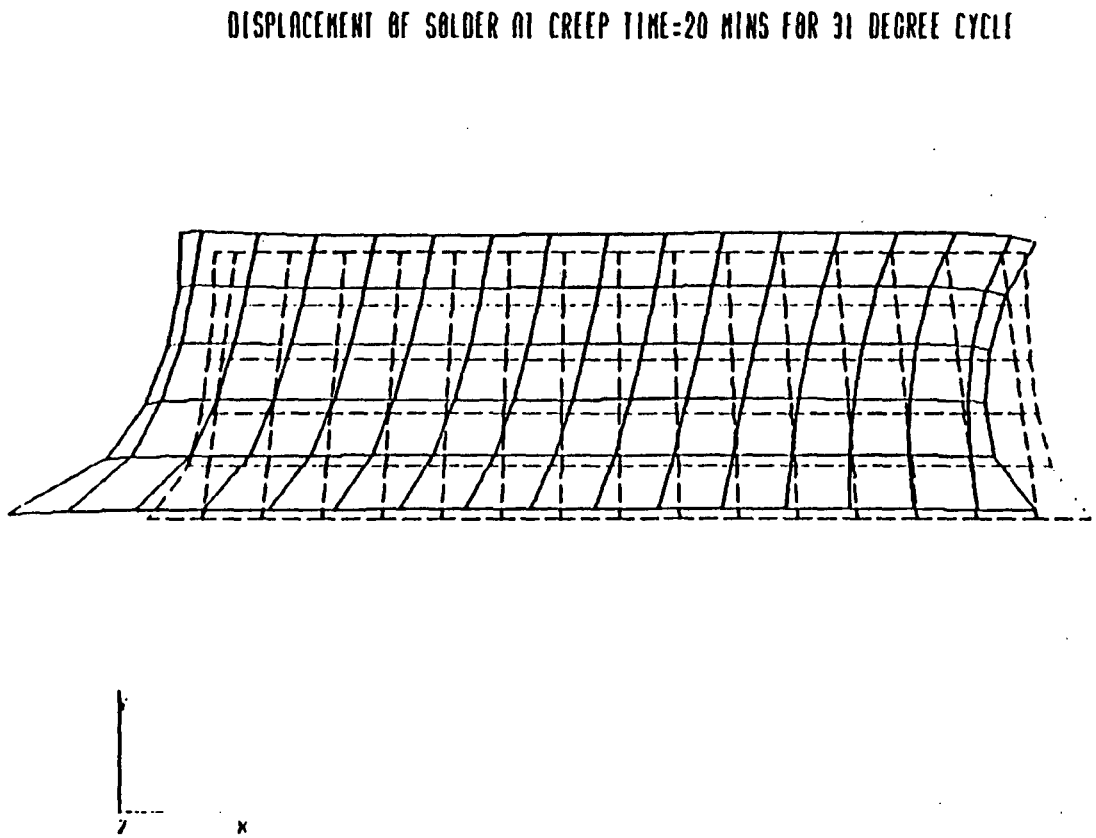

Figure 5b: Solder deformation after 20 min. dwell at T = 55.5°C

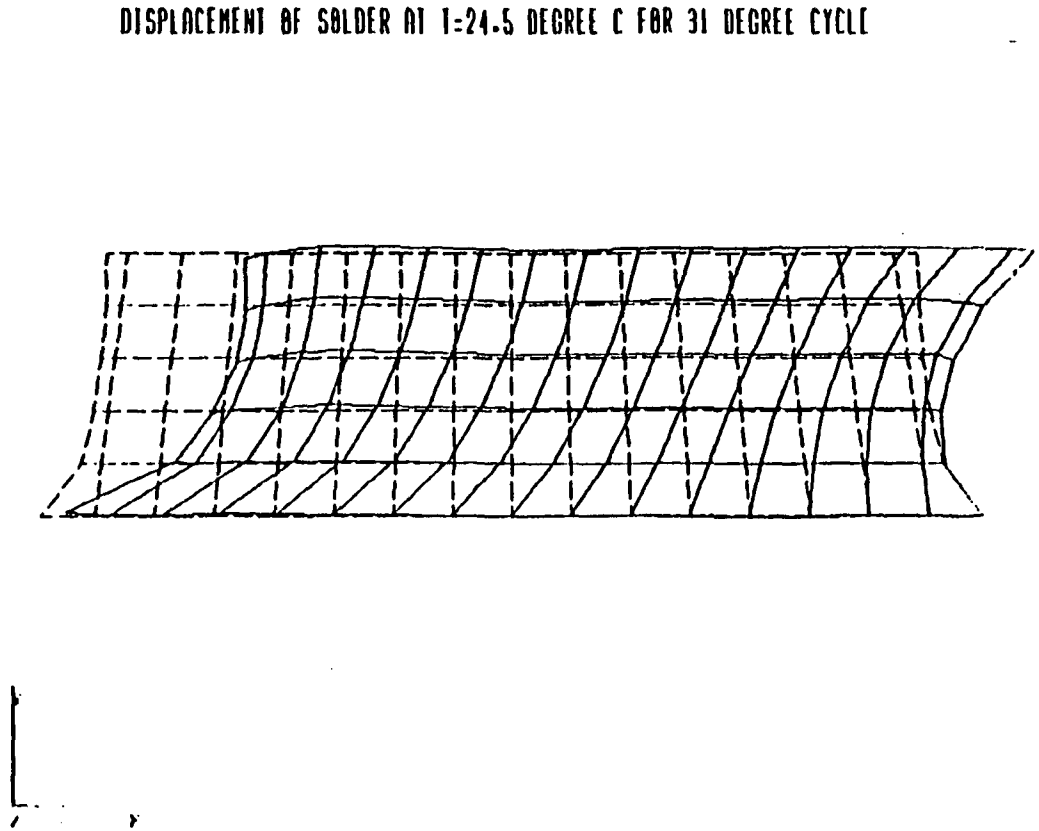

Figure 5c: Solder deformation after unloading to T = 24.5°C.

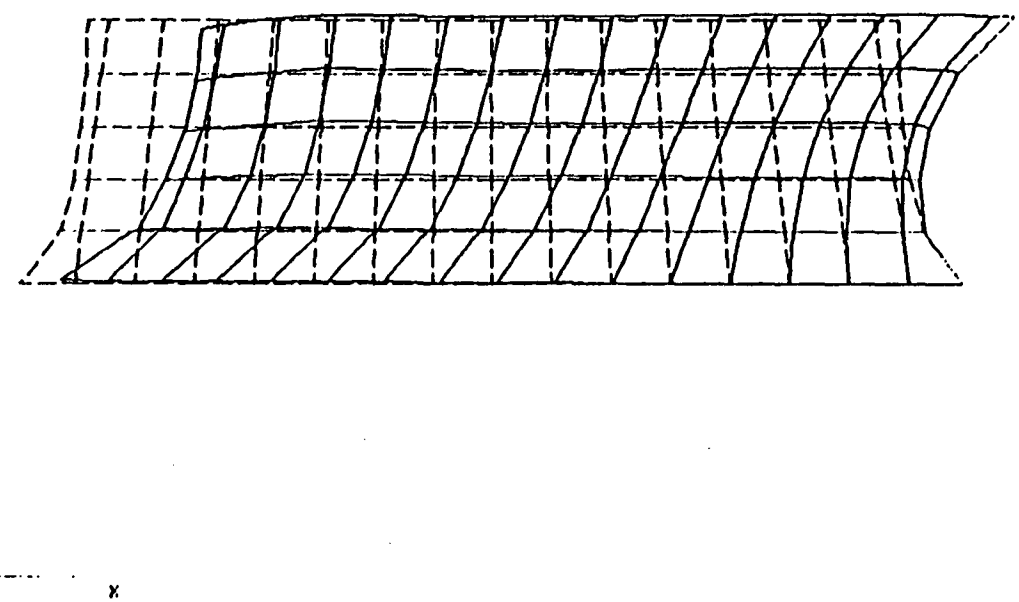

Figure 5d: Solder deformation after 20 min. dwell at T = 24.5°C.

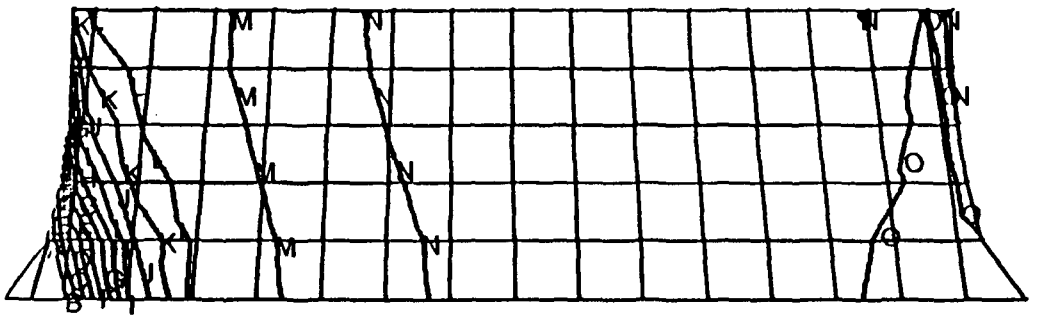

.00805= A

.00750= B

.00695= C

.00640= D

.00586= E

.00531= F

.00476= G

.00421= H

.00366= I

.00311= J

.00256= K

.00201= L

.00146= M

.000914= N

.000365= O

Figure 6a: Maximum shear strain in solder after loading to T = 55.5°C

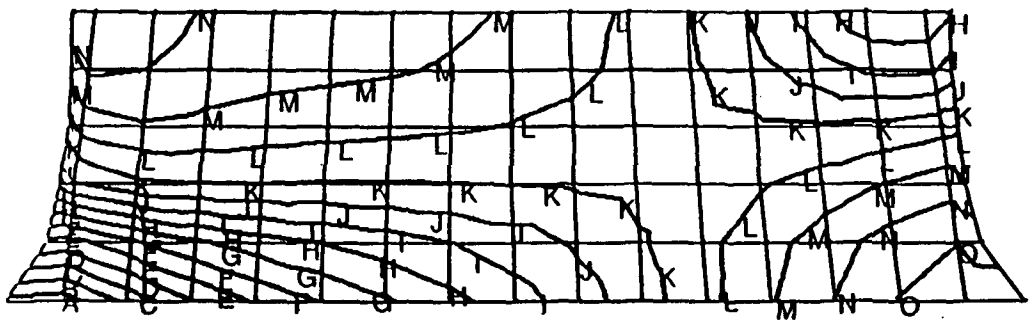

.0360= A

.0335= B

.0311= C

.0286= D

.0262= E

.0237= F

.0213= G

.0188= H

.0164= I

.0139= J

.0115= K

.00903= L

.00658= M

.00413= N

.00168= O

Figure 6b: Maximum shear strain in solder after 20 min. dwell at T = 55.5°C.

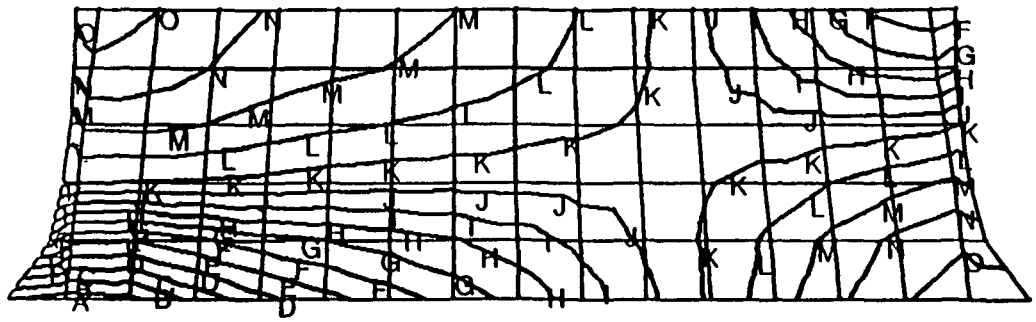

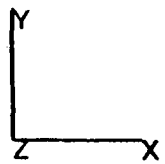

.0295= A

.0275= B

.0255= C

.0235= D

.0214= E

.0194= F

.0174= G

.0154= H

.0134= I

.0114= J

.00935= K

.00734= L

.00532= M

.00331= N

.00129= O

Figure 6c: Maximum shear strain in solder after unloading to T = 24.5°C.

.0213= A

.0198= B

.0184= C

.0169= D

.0155= E

.0140= F

.0125= G

.0111= H

.00963= I

.00817= J

.00672= K

.00526= L

.00380= M

.00234= N

.000888= O

Figure 6d: Maximum shear strain in solder after 20 min. dwell at T = 24.5°C.

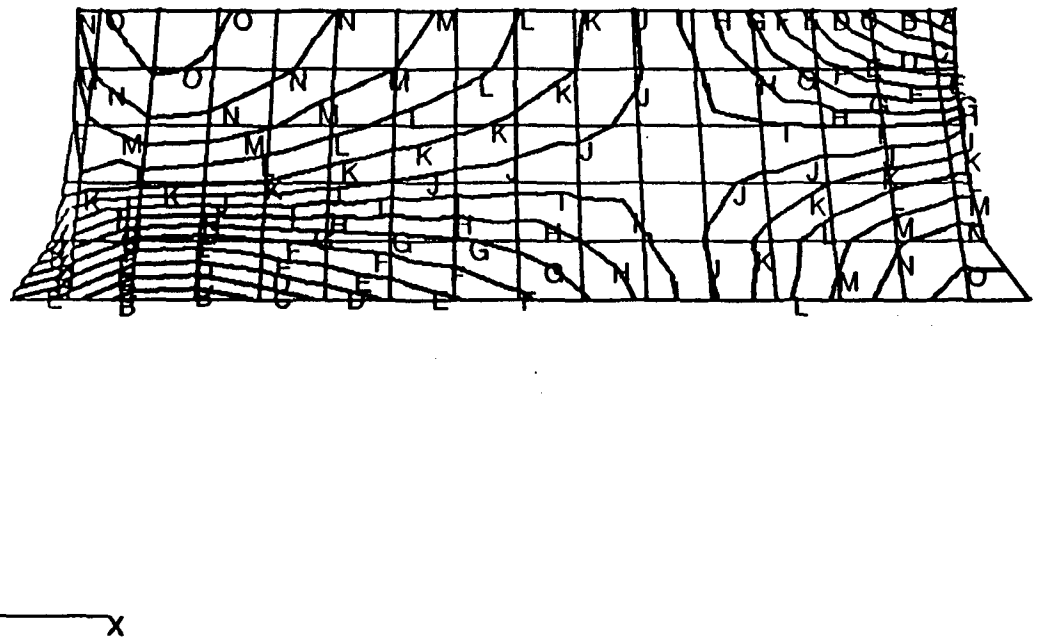

Figure 7: Maximum principal strain in solder after 20 min. dwell at T = 24.5°C.

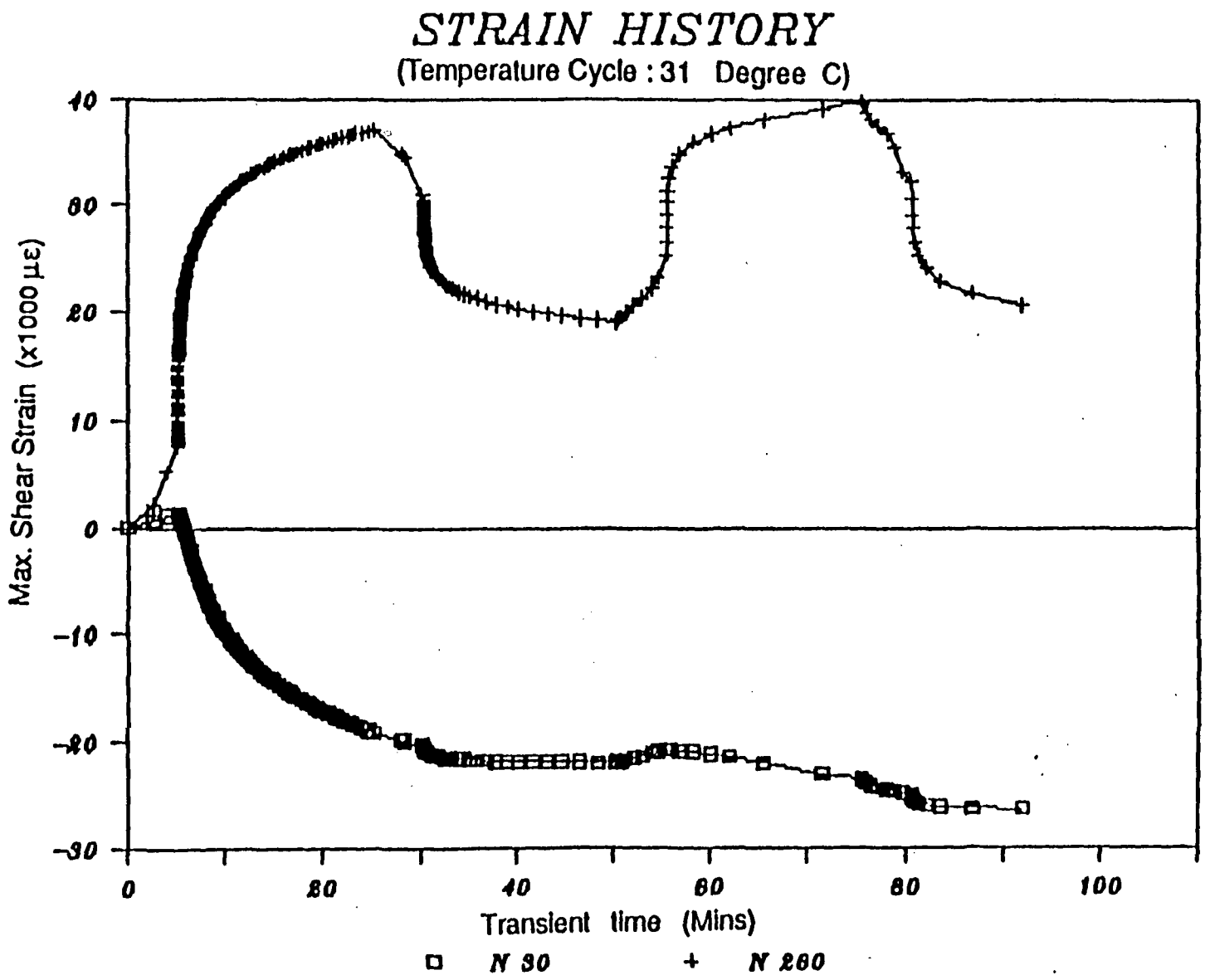

Figure 8: Maximum shear strain history at nodes 260 and 30 for two cycles at cyclic temperature change of 31° C:

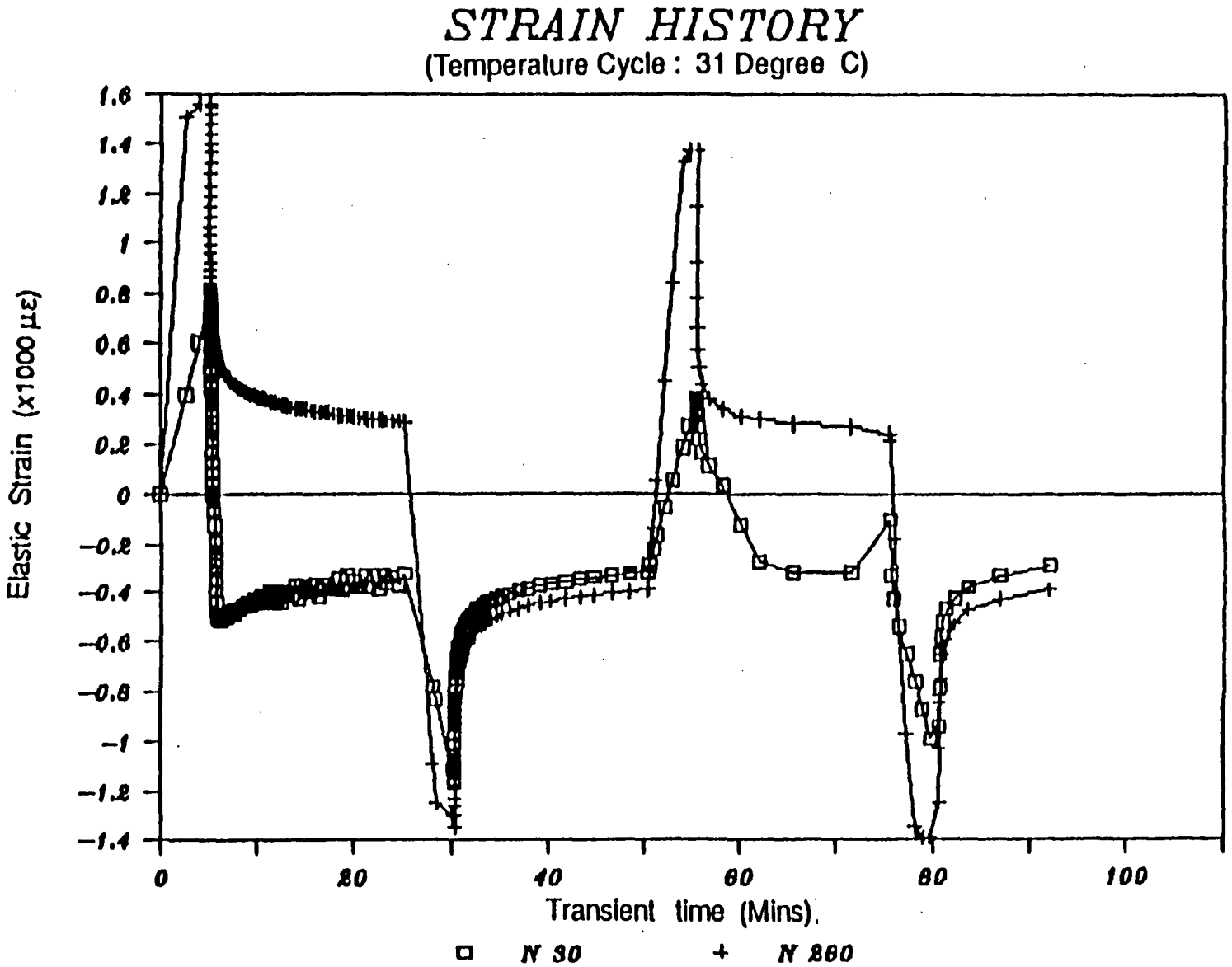

Figure 9a: Elastic equivalent strain history at nodes 260 and 30 for two cycles at a cyclic temperature change of 31° C.

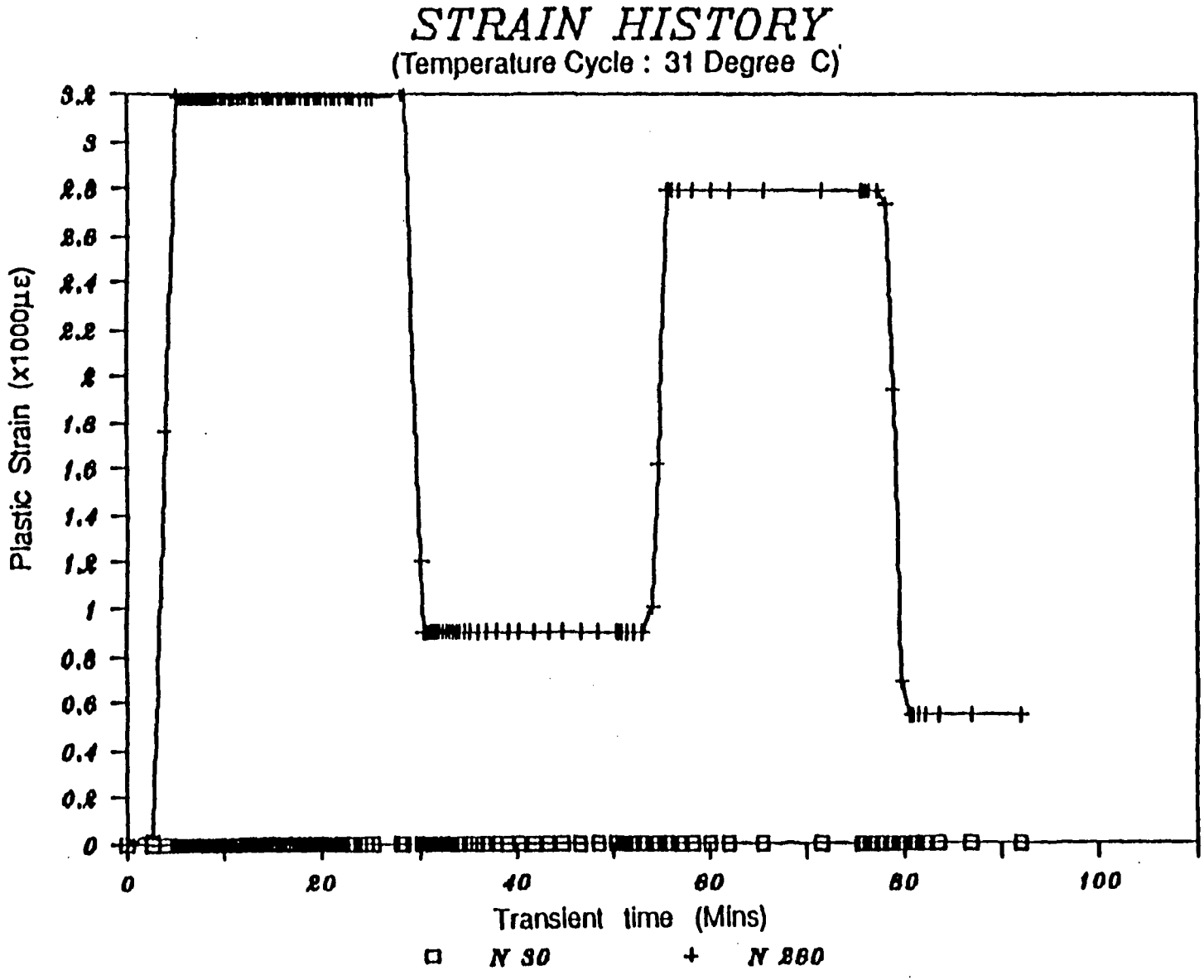

Figure 9b: Plastic equivalent strain history at nodes 260 and 30 for two cycles at a cyclic temperature change of 31°C.

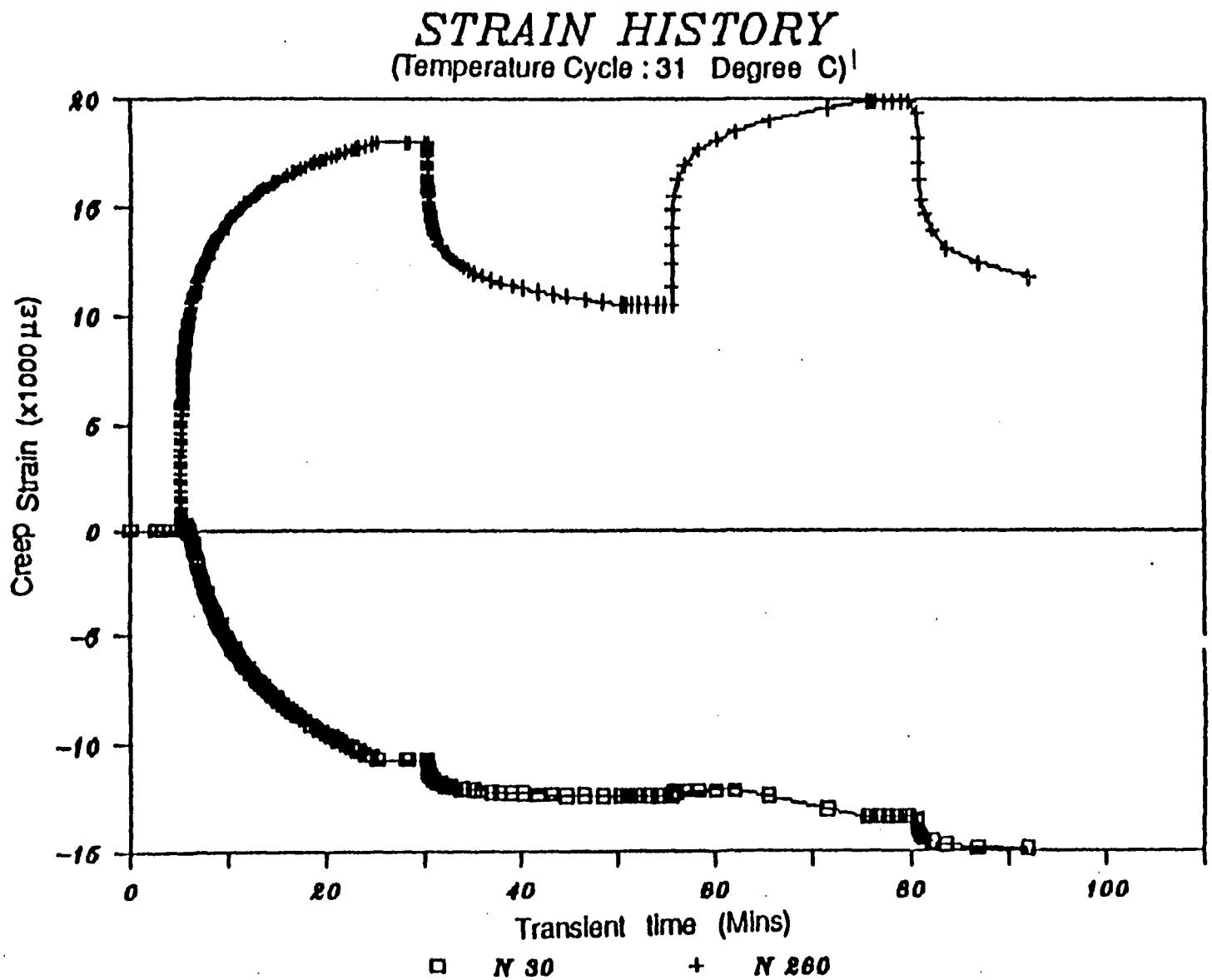

Figure 9c: Creep equivalent strain history at nodes 260 and 30 for two cycles at a cyclic temperature change of 31°C.

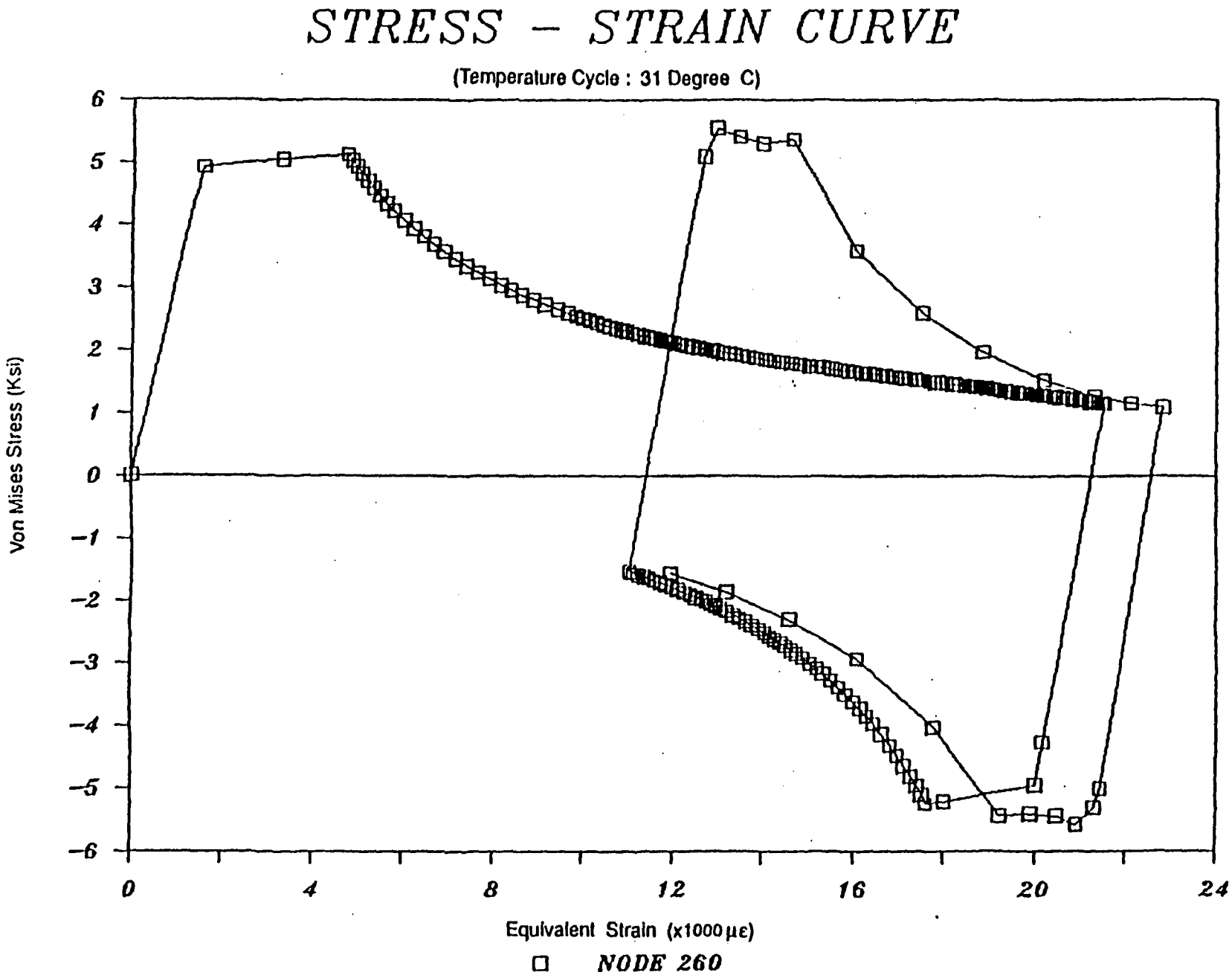

Figure 10a : Hysteresis loop at node 260 for two cycles at a cyclic temperature change of 31° C.

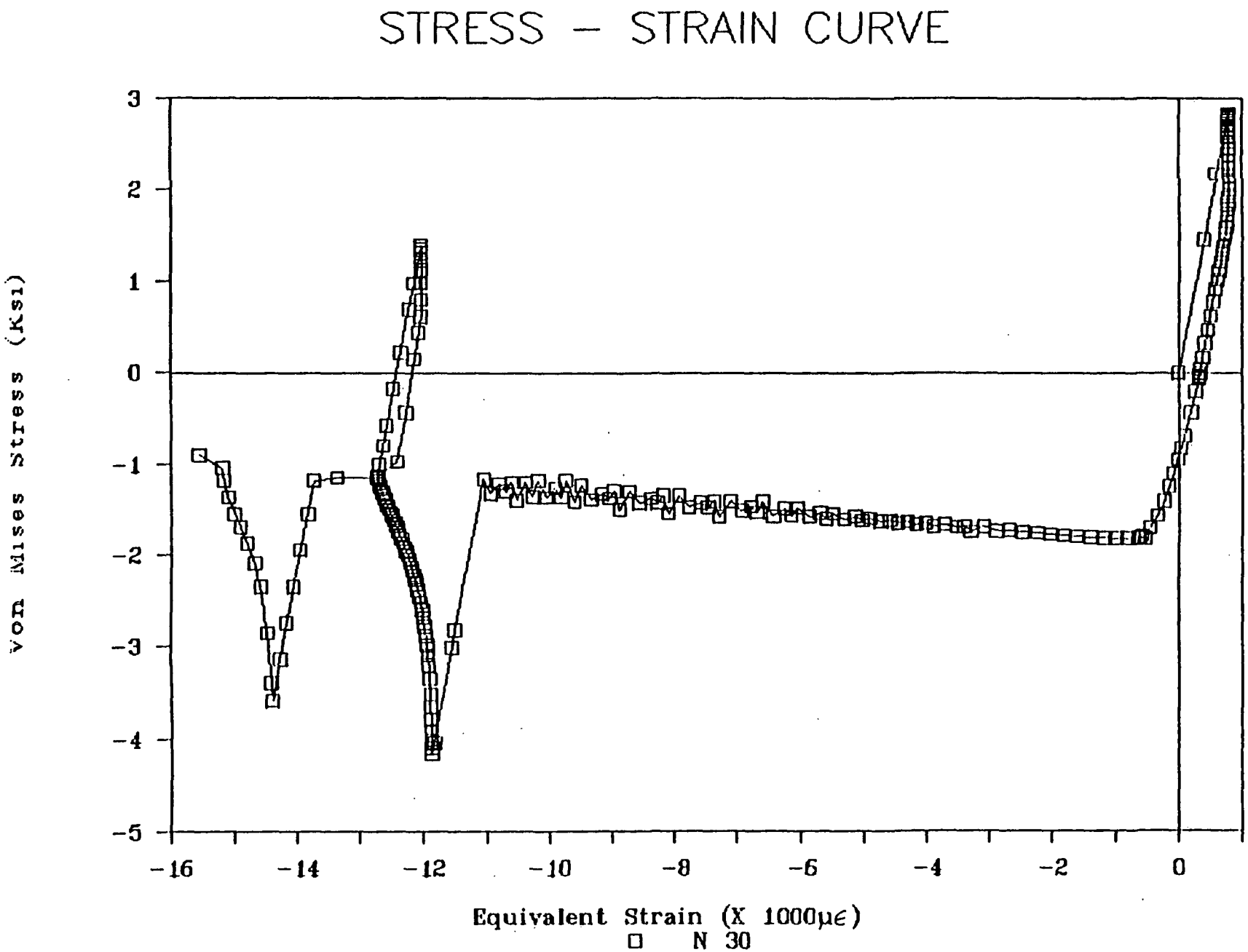

Figure 10b : Hysteresis loop at node 30 for two cycles at a cyclic temperature change of 31° C.

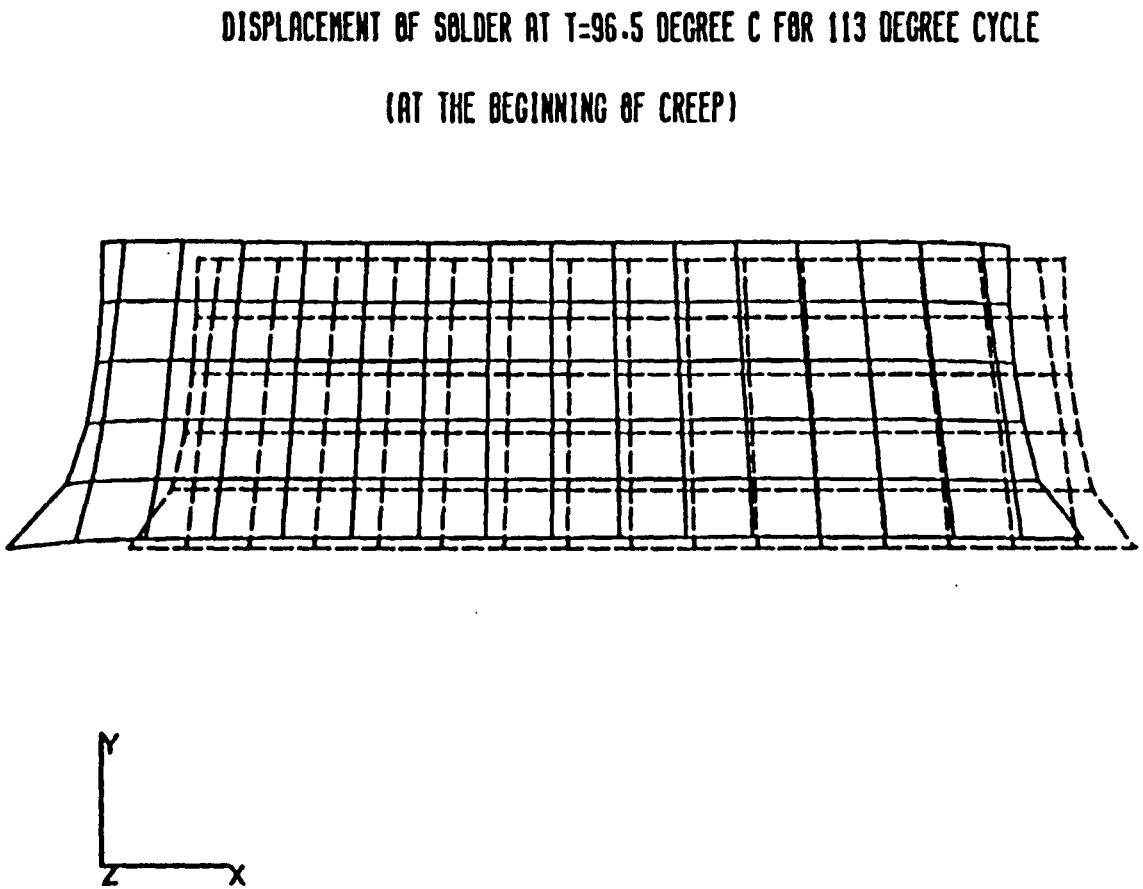

Figure 11a : Solder deformation after loading to T=96.5° C

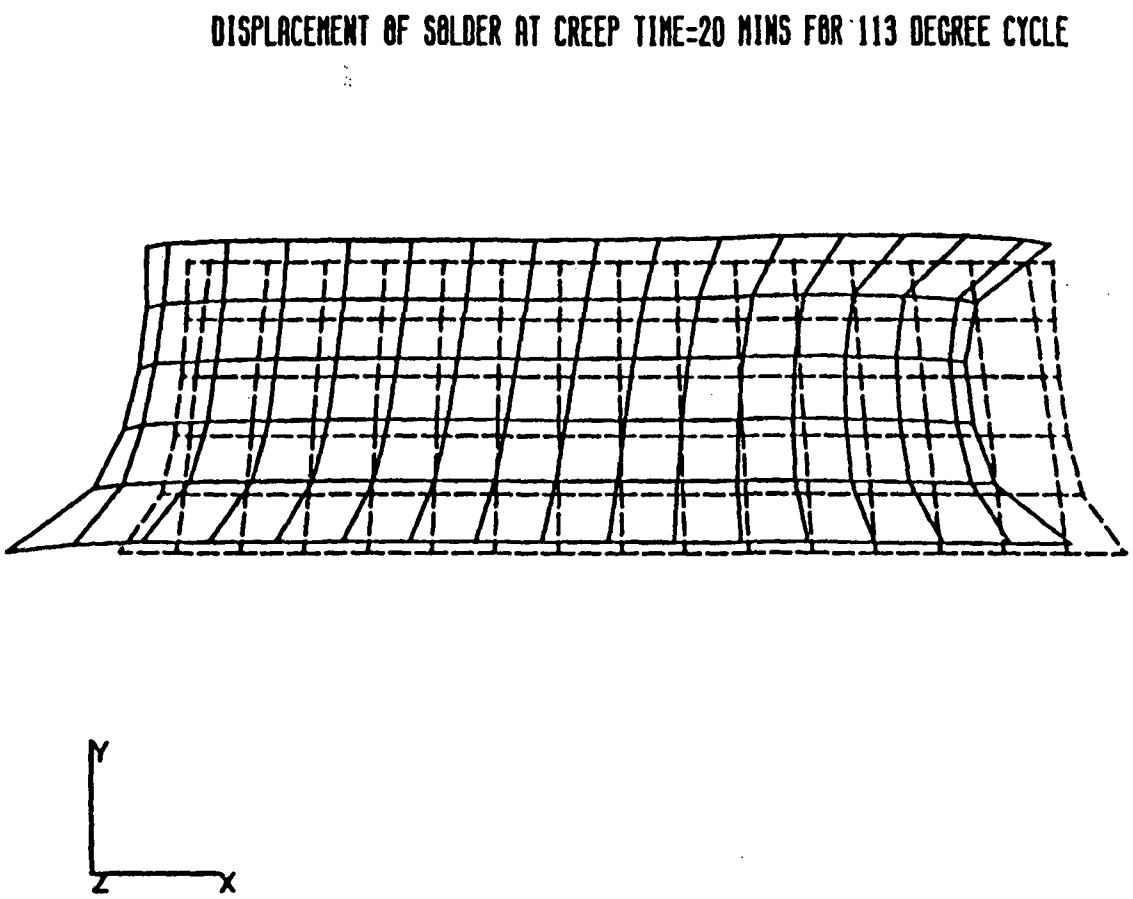

Figure 11b : Solder deformation after 20 min. dwell at T=96.5° C

DISPLACEMENT OF SOLDER AT T=-16.5 DEGREE C (UNLOADING)

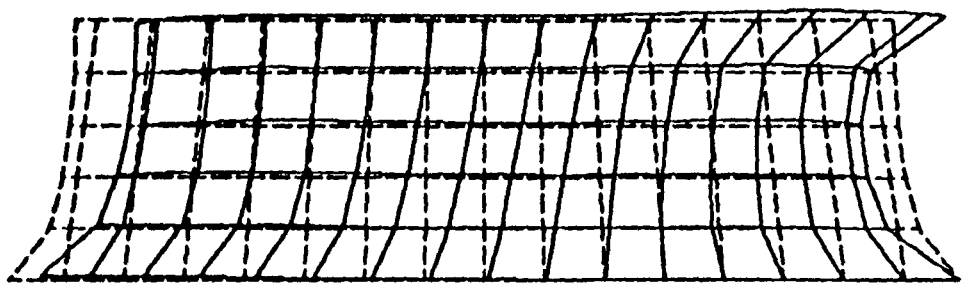

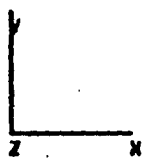

PROJECT CREEP
PATRAN POST-PROCESS FILE CREATED BY MARPAT3.0 24-OCT-98 14:19:0
TIME = 0.120000E+04 FREQUENCY = 0.000000E+00 GENERALIZED MASS = 0.000

Figure 11c : Solder deformation after unloading to T=-16.5^{o} C

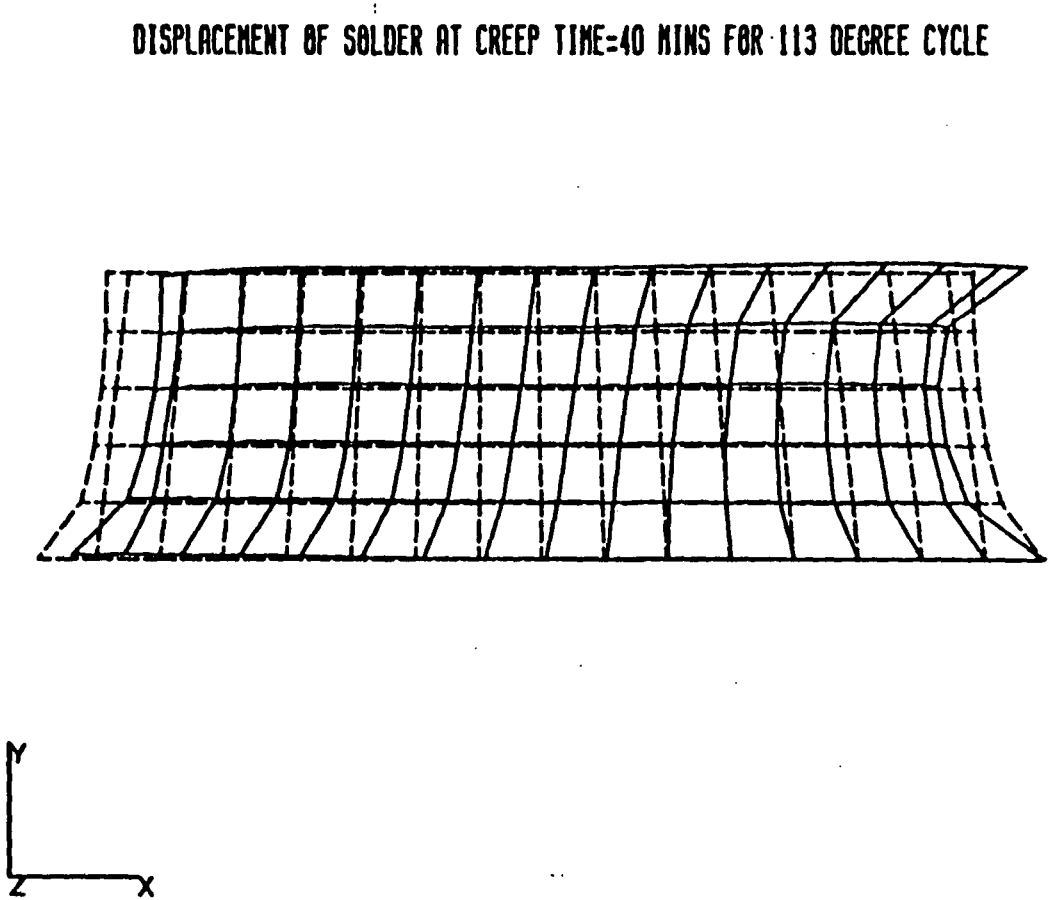

Figure 11d : Solder deformation after 20 min. dwell at T=-16.5° C

MAX. SHEAR STRAIN AT T=96.5 DEGREE C FOR 113 DEGREE CYCLE

(AT THE BEGINNING OF CREEP)

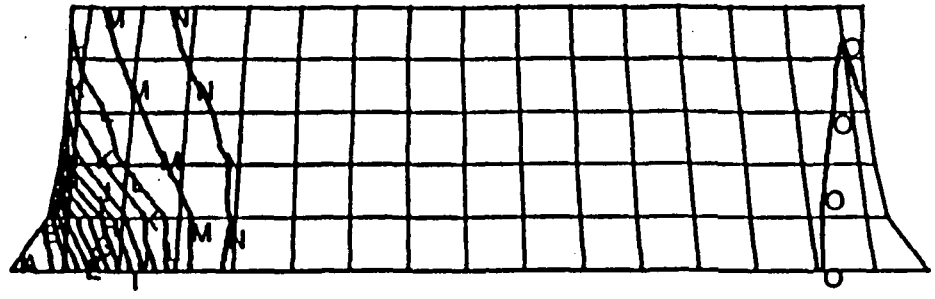

.0285= A

.0266= B

.0246= C

.0226= D

.0207= E

.0187= F

.0168= G

.0148= H

.0129= I

.0109= J

.00897= K

.00701= L

.00506= M

.00311= N

.00115= O

Figure 12a : Maximum shear strain in solder after loading to T=96.5° C

MAX. SHEAR STRAIN AT CREEP TIME=20 MINS FOR 113 DEGREE CYCLE

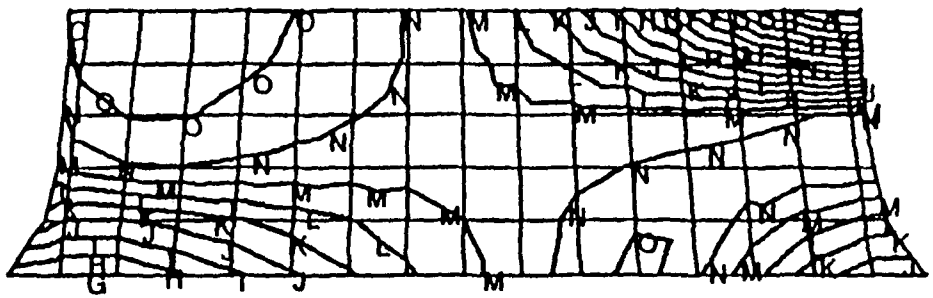

.185= A

.173= B

.160= C

.148= D

.135= E

.123= F

.110= G

.0974= H

.0848= I

.0722= J

.0596= K

.0470= L

.0344= M

.0219= N

.00927= O

Figure 12b : Maximum shear strain in solder after 20 min. dwell at T=96.5° C

MAX. SHEAR STRAIN AT T=-16.5 DEGREE C FOR 113 DEGREE CYCLE

(UNLOADING WITH THE CREEP EFFECT)

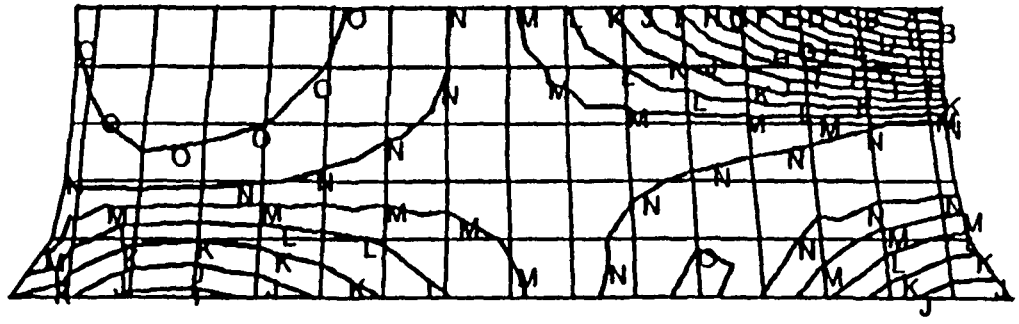

.187= A

.174= B

.161= C

.149= D

.136= E

.123= F

.110= G

.0976= H

.0848= I

.0720= J

.0593= K

.0465= L

.0337= M

.0210= N

.00818= O

Figure 12c : Maximum shear strain in solder after unloading to T=-16.5° C

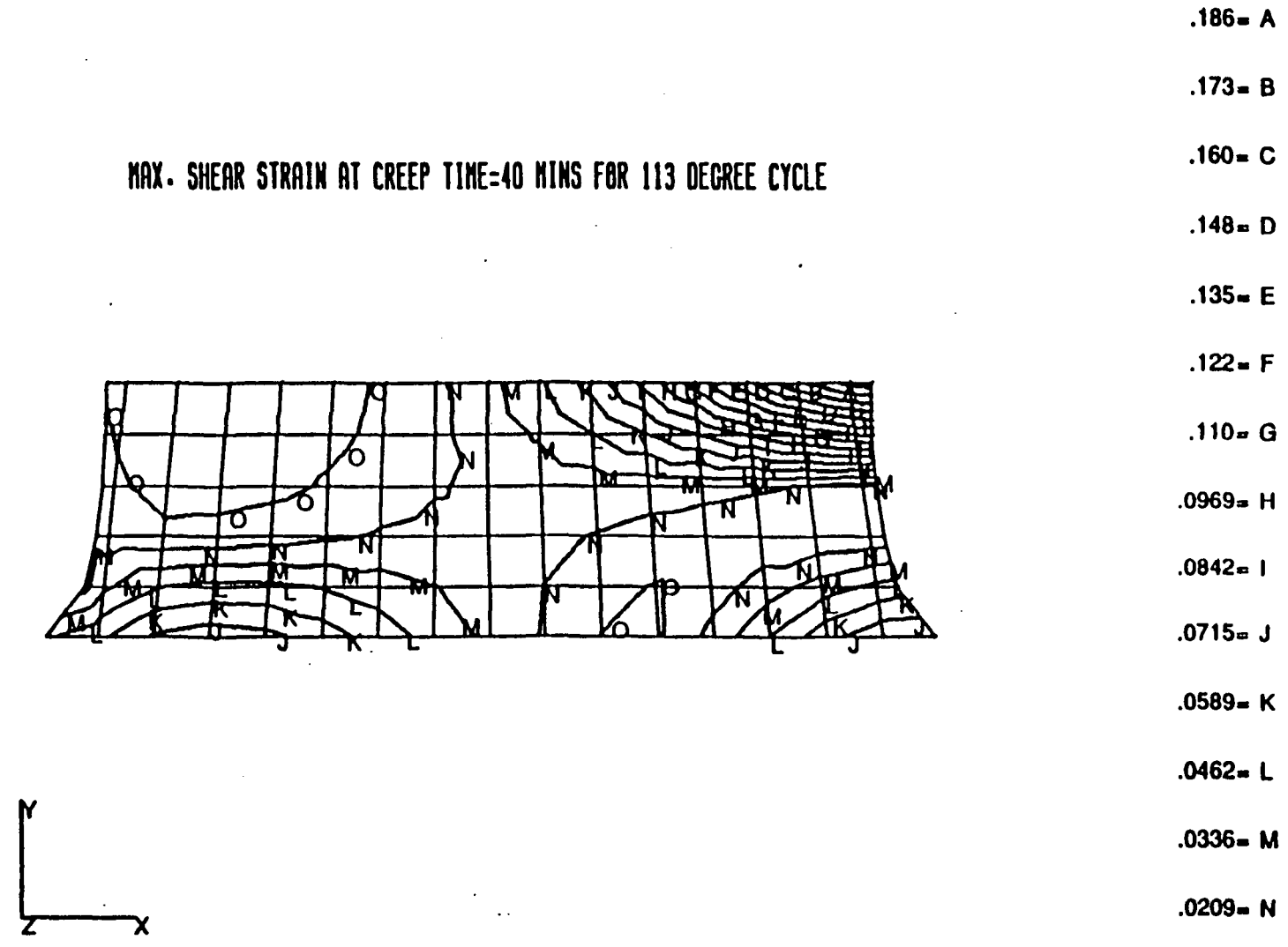

Figure 12d : Maximum shear strain in solder after 20 min. dwell at T=-16.5° C

MAX. PRINCIPAL STRAIN AT CREEP TIME=40 MINS FOR 113 DEGREE CYCLE

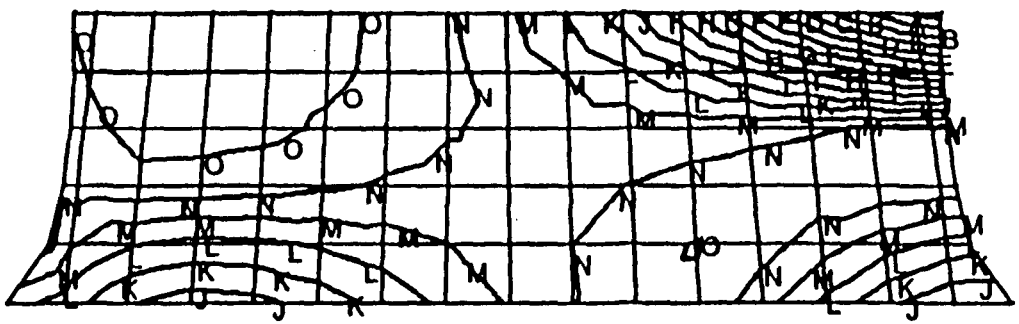

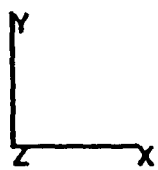

.0932= A

.0868= B

.0804= C

.0740= D

.0676= E

.0612= F

.0548= G

.0484= H

.0419= I

.0355= J

.0291= K

.0227= L

.0163= M

.00988= N

.00347= O

Figure 13 : Maximum principal strain in solder after 20 min. dwell at T=-16.5° C

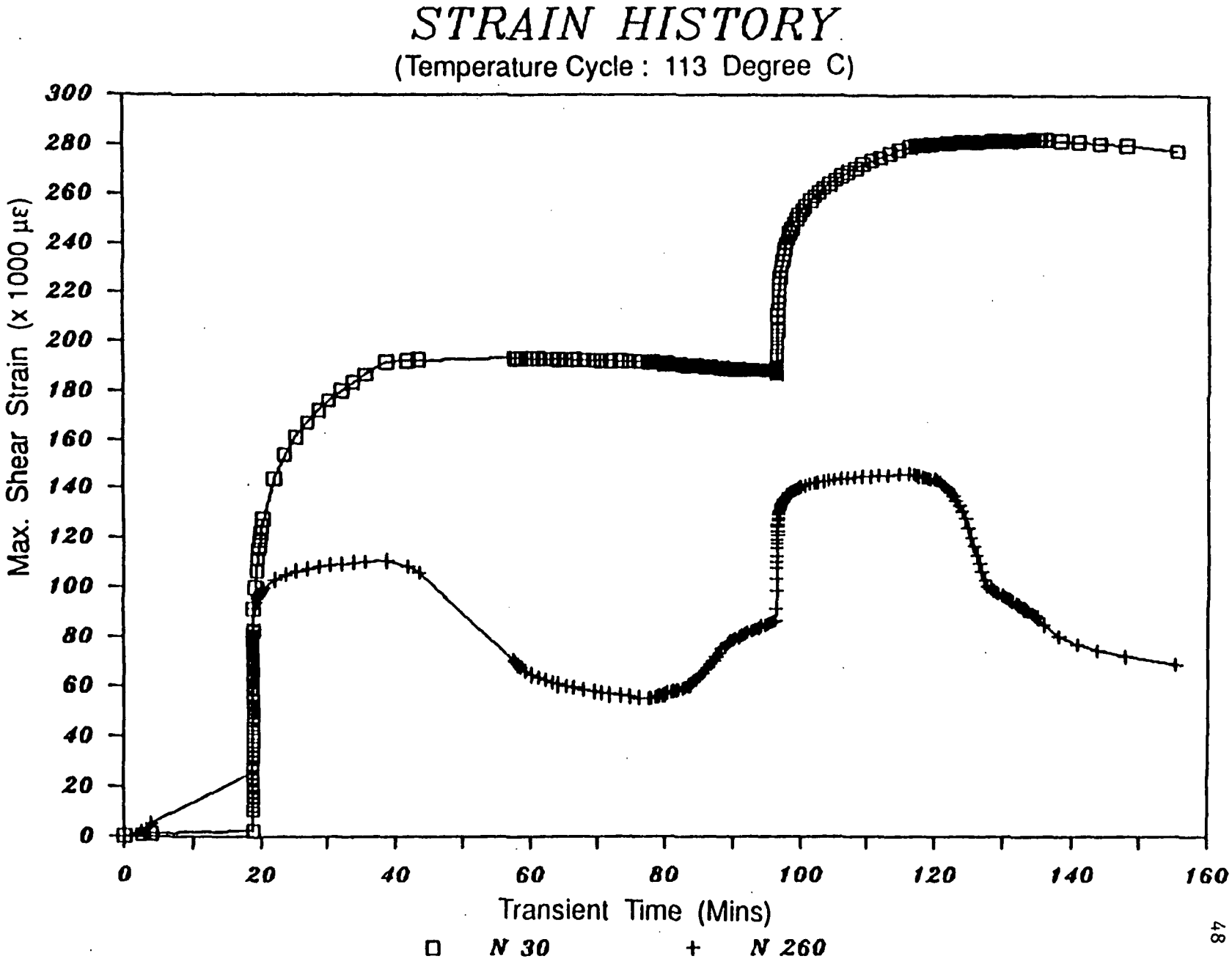

Figure 14 : Maximum shear strain history at node 260 and 30 for two cycles at cyclic temperature change of 113°C

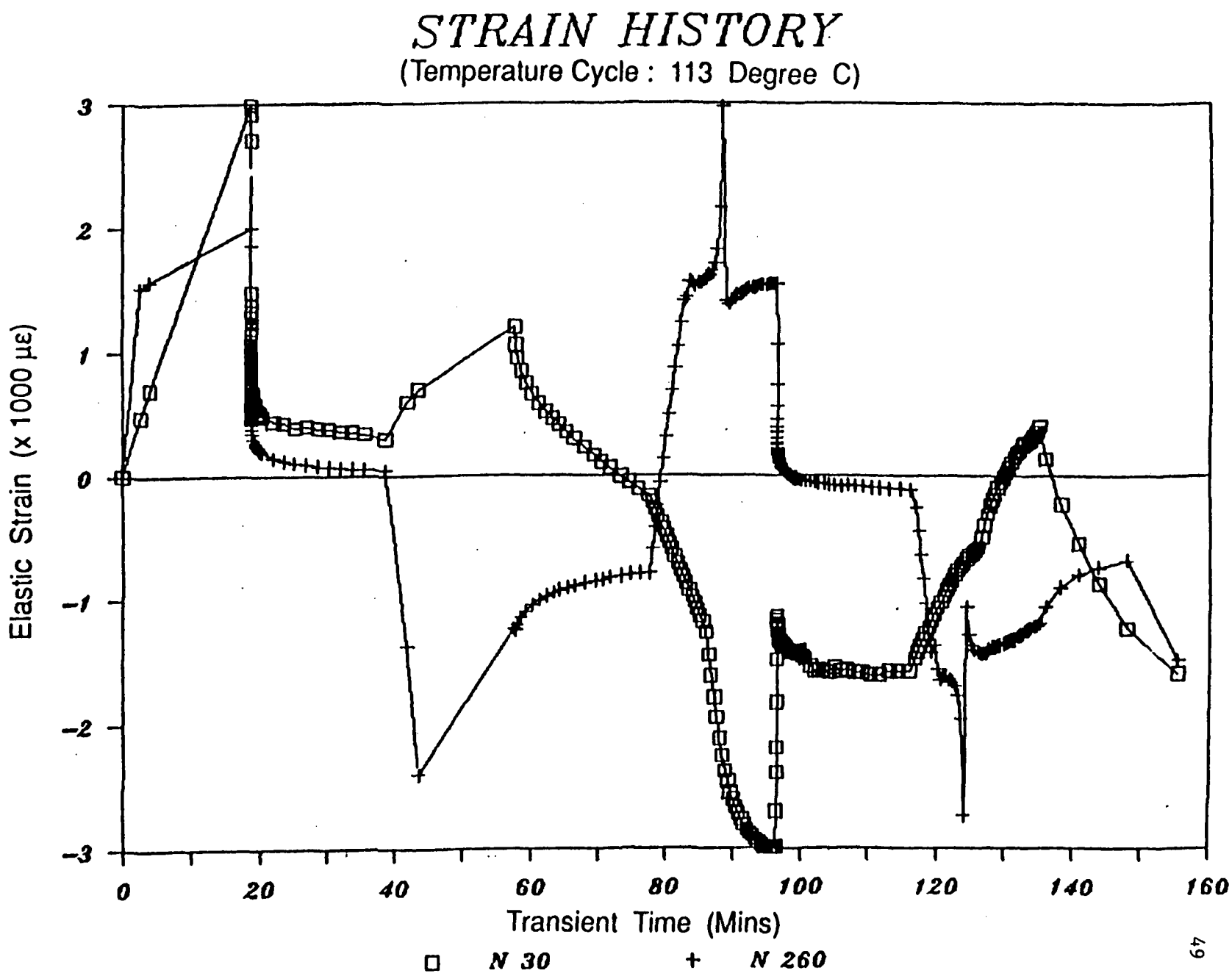

Figure 15a : Elastic equivalent strain history at node 260 and 30 for two cycles at cyclic temperature change of 113°C

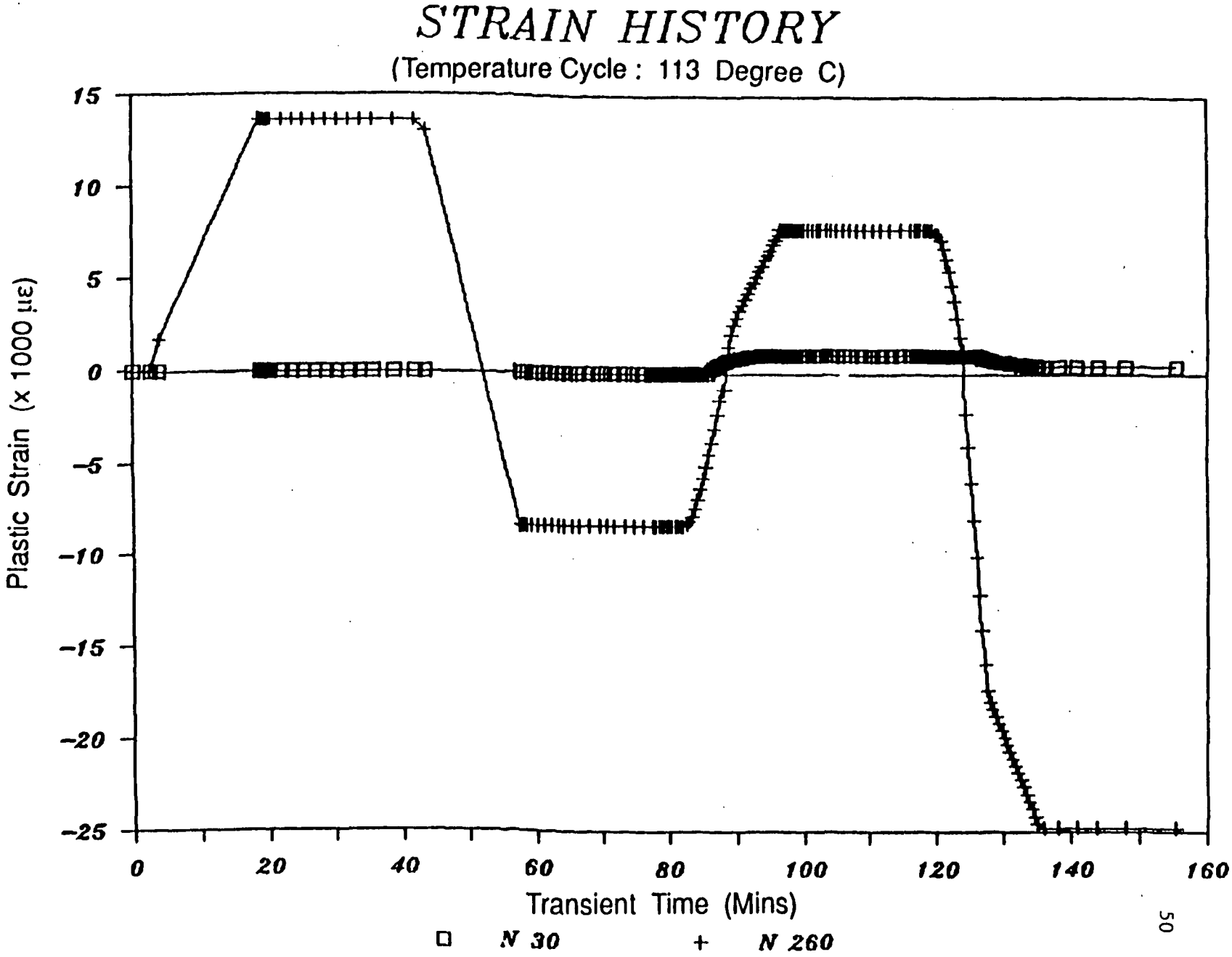

Figure 15b : Plastic equivalent strain history at node 260 and 30 for two cycles at cyclic temperature change of 113°C

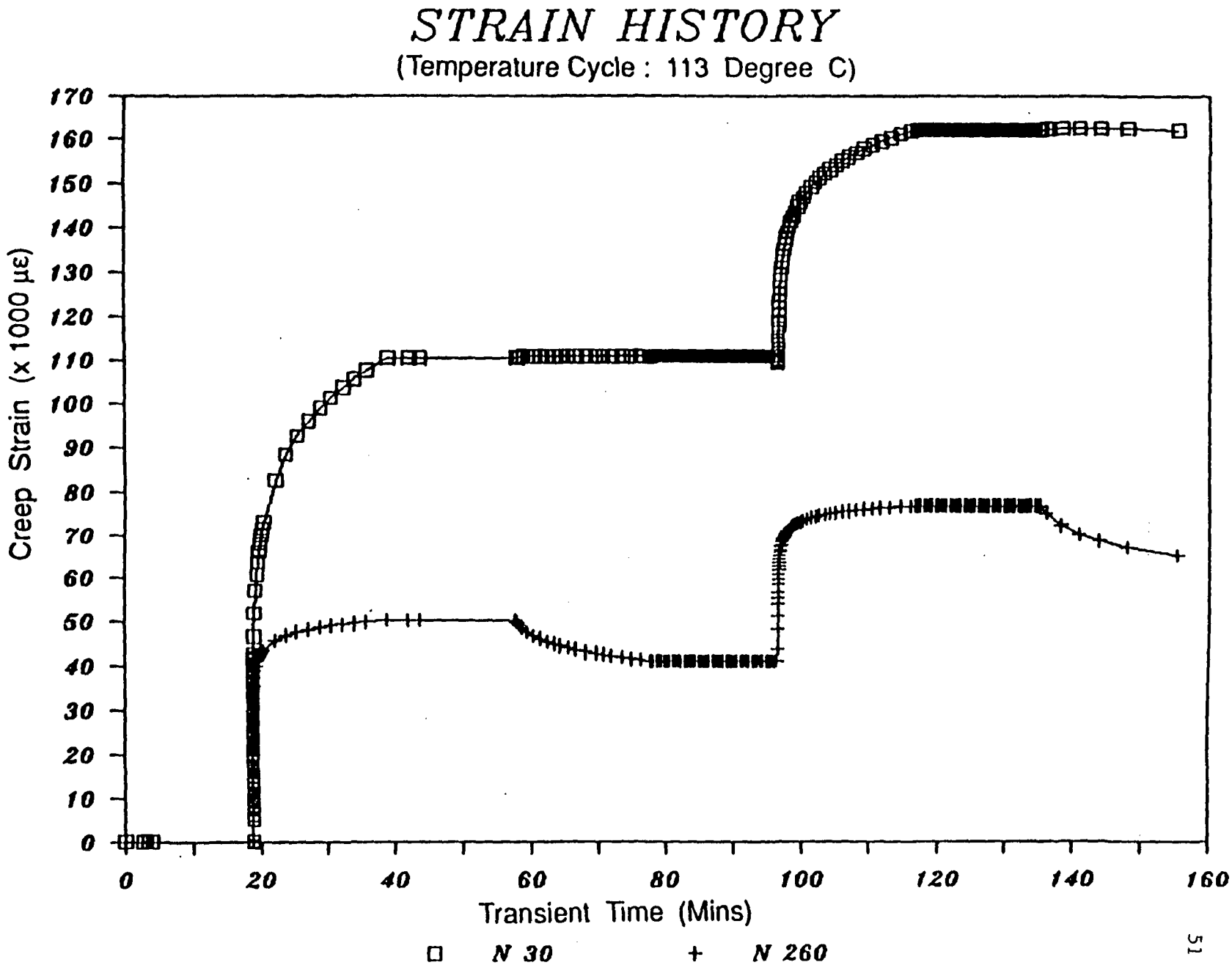

Figure 15c : Creep equivalent strain history at node 260 and 30 for two cycles at cyclic temperature change of 113°C

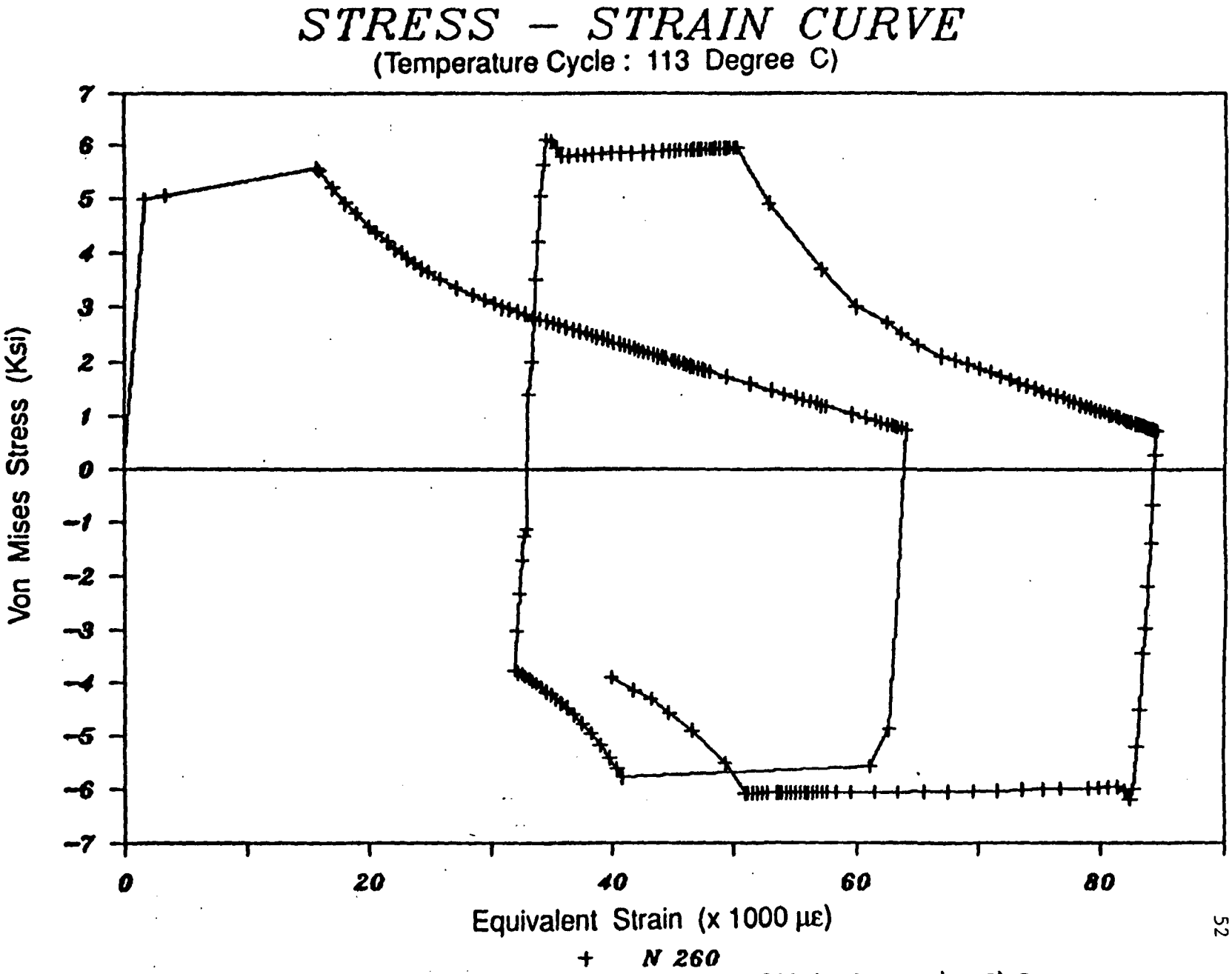

Figure 16a : Hysteresis loop at node 260 for two cycles at a cyclic temperature of 113° C

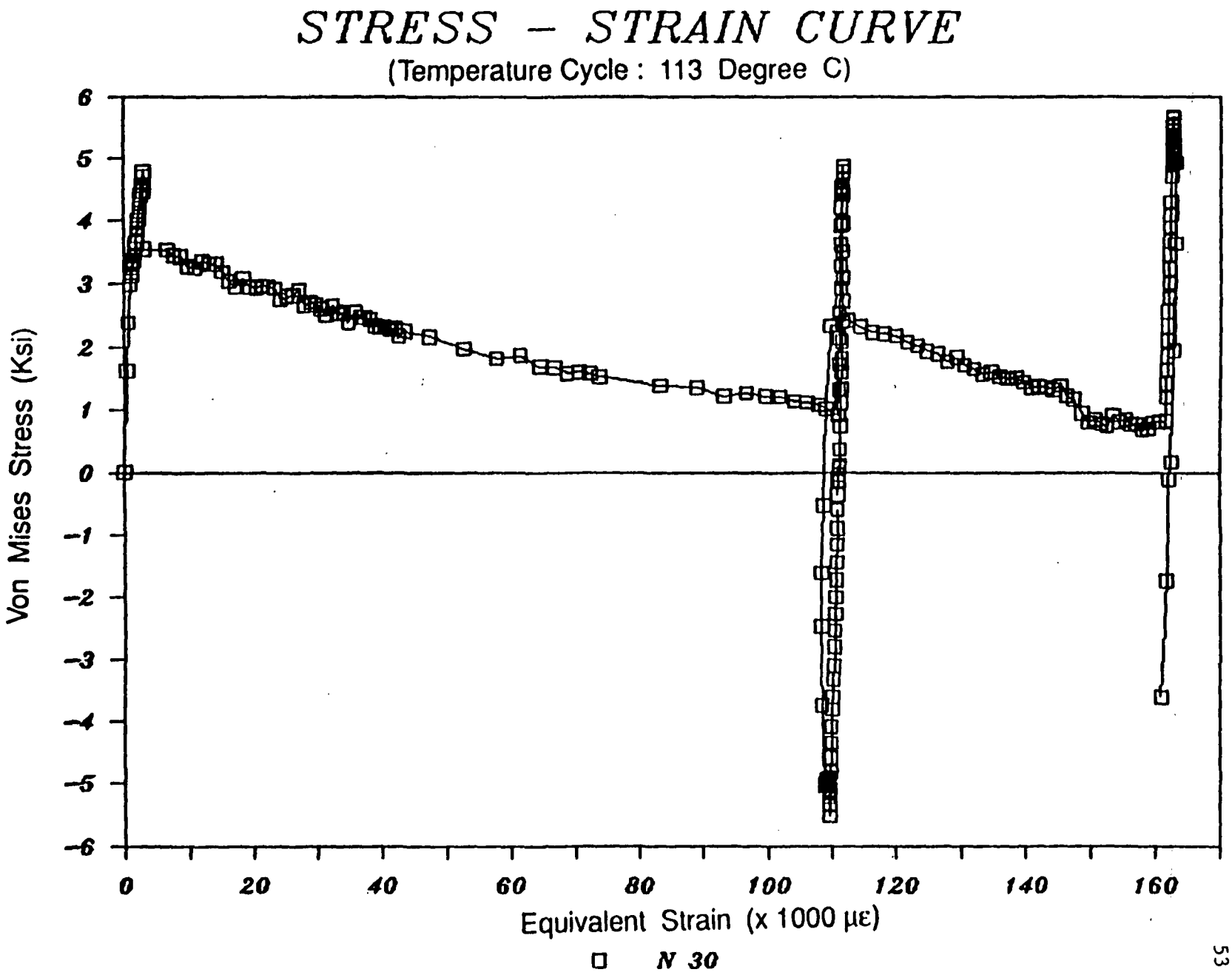

Figure 16b : Hysteresis loop at node 30 for two cycles at a cyclic temperature of 113° C